VŠB – Technical University of Ostrava

Thermal conductivity of actinides and actinide compounds

Tepelná vodivost aktinoidů a aktinoidových sloučenin

2020

Author: Bc. *et* Bc. Lukáš Kývala
Supervisor: Ing. Dominik Legut Ph.D.

VŠB - Technical University of Ostrava
University Study Programmes
CNT - Nanotechnology Centre

Diploma Thesis Assignment

Student:	**Bc. et Bc. Lukáš Kývala**
Study Programme:	N3942 Nanotechnology
Study Branch:	3942T001 Nanotechnology
Title:	Thermal conductivity of actinide compounds Tepelná vodivost aktinidů a aktinidiových sloučenin
The thesis language:	English

Description:

The actinide carbides can be used as advanced nuclear fuels for the so-called generation IV reactors (including the gas-cooled and sodium-cooled fast reactors). These carbides are promising because of higher thermal conductivity and operational temperature (more efficient heat transfer) over conventional oxide fuels (e.g. UO2). The actinides pose 5f electrons, which are crucial for electronic structure and lattice dynamics. The primary goal for the diploma thesis is the investigation of the thermal conductivity in actinide metals and actinide compounds. Thermal conductivity is, to a large extent, based on the possibility of calculation of the force constants to the third order and, hence, finding of such an electronic structure model with high accuracy. Using thermal conductivity analysis, along with the increasing temperature, the largest contribution is identified, i.e. coming from phonons or electrons. Next, the phase stability is determined for newly discovered actinide phases.

References:

MANES, L. Actinides - Chemistry and Physical Properties. Berlin, Heidelberg: Springer-Verlag, 1985. ISBN 9783540390428.

MARTIN, R. M., Electronic Structure: Basic Theory and Practical Methods, Cambridge University Press, 2004, ISBN-13: 978-0521782852.

ASCROFT N. W. and N. D. Mermin, Solid State Physics, Cengage Learning, 1976, ISBN-13: 978-0030839931.

KAXIRAS, Efthimios. Atomic and electronic structure of solids. New York: Cambridge University Press, 2003. ISBN 978-0521523394.

CHAIKIN, P. M. and T. C. LUBENSKY. Principles of condensed matter physics. Cambridge [u.a.]: Cambridge Univ. Press, 2007. ISBN 9780521794503.

SINGLETON, J., Band Theory and Electronic Properties of Solids, Oxford Master Series in Physics, 2001, ISBN-10: 0198505914.

BLUNDELL, Stephen. Magnetism in condensed matter. Oxford: Oxford University Press, 2001. Oxford master series in condensed matter physics. ISBN 9780198505914.

GRIMVALL, Göran. Thermophysical properties of materials. Enl. and rev. ed. New York:

Elsevier, 1999. ISBN 0444827943.

Extent and terms of a thesis are specified in directions for its elaboration that are opened to the public on the web sites of the faculty.

Supervisor: **Ing. Dominik Legut, Ph.D.**

Date of issue: 02.12.2019

Date of submission: 08.05.2020

prof. Ing. Jaromír Pištora, CSc.
Head of Department

Ing. Zdeňka Chmelíková, Ph.D.
Vice-rectress for Study Affairs

Zásady pro vypracování diplomové práce

I.

Diplomovou prací (dále jen DP) se ověřují vědomosti a dovednosti, které student získal během studia, a jeho schopnosti využívat je při řešení teoretických i praktických problémů.

II.

Uspořádání diplomové práce:

1. Titulní list
2. Originál zadání DP
3. Zásady pro vypracování DP
4. Prohlášení + místopřísežné prohlášení
5. Prohlášení spolupracující právnické nebo fyzické osoby o souhlasu se zveřejněním DP
6. Abstrakt + klíčová slova česky a anglicky
7. Obsah DP
8. Textová část DP
9. Seznam použité literatury
10. Přílohy

ad 1) Titulní list je koncipován podle požadavků příslušné oborové katedry.

ad 2) Originál zadání DP student obdrží na své oborové katedře.

ad 3) Tyto „Zásady pro vypracování diplomové práce“ následují za originálem zadání DP.

ad 4) Prohlášení + místopřísežné prohlášení napsané na zvláštním a vlastnoručně podepsané studentem s uvedením data odevzdání DP.

ad 5) V případě, že DP vychází ze spolupráce s jinými právnickými a fyzickými osobami a obsahuje citlivé údaje, je na zvláštním listě vloženo prohlášení spolupracující právnické nebo fyzické osoby o souhlasu se zveřejněním DP.

ad 6) Abstrakt a klíčová slova jsou uvedena na zvláštním listu česky a anglicky v rozsahu max. 1 strany pro obě jazykové verze.

ad 7) Obsah DP se uvádí na zvláštním listu. Zahrnuje názvy všech očíslovaných kapitol, podkapitol a statí textové části DP, odkaz na seznam příloh a seznam použité literatury s uvedením příslušné stránky. Předpokládá se desetinné číslování.

ad 8) Textová část DP obvykle zahrnuje:

- Úvod, obsahující charakteristiku řešeného problému a cíle jeho řešení v souladu se zadáním DP;
- Vlastní rozpracování DP (včetně obrázků, tabulek, výpočtů) s dílčími závěry vhodně členěné do kapitol a podkapitol podle povahy problému;
- Závěr, obsahující celkové hodnocení výsledků DP z hlediska stanoveného zadání.

DP bude zpracována v rozsahu min. cca 45 stran (včetně obsahu a seznamu použité literatury).

Text musí být napsán vhodným textovým editorem počítače po jedné straně bílého nelesklého papíru formátu A4 při respektování následující doporučené úpravy - písmo Times New Roman 12b; řádkování 1,5; okraje – horní, dolní – 2,5 cm, levý – 3 cm, pravý 2 cm. Fotografie, schémata, obrázky, tabulky musí být očíslovány a musí na ně být v textu poukázáno. Budou zařazeny průběžně v textu, pouze je-li to nezbytně nutné, jako přílohy (viz ad 10).

Odborná terminologie práce musí odpovídat platným normám. Všechny výpočty musí být přehledně uspořádány tak, aby každý odborník byl schopen přezkoušet jejich správnost. Matematické vzorce musí být číslovány (v kulatých závorkách). U vzorců, údajů a hodnot převzatých z odborné literatury nebo z praxe musí být uveden jejich pramen - u literatury citován číselným odkazem (v hranatých závorkách) na seznam použité literatury. Nedostatky ve způsobu vyjadřování, nedostatky gramatické, neopravené chyby v textu mohou snížit klasifikaci práce.

ad 9) DP bude obsahovat alespoň 15 literárních odkazů, z toho nejméně 5 v některém ze světových jazyků. Seznam použité literatury se píše na zvláštním listě. Citaci literatury je nutno uvádět důsledně v souladu s ČSN ISO 690. Na práce uvedené v seznamu použité literatury musí být uveden odkaz v textu DP.

ad 10) Přílohy budou obsahovat jen ty části (speciální výpočty, zdrojové texty programů aj.), které nelze vhodně včlenit do vlastní textové části např. z důvodu ztráty srozumitelnosti.

III.

Diplomovou práci student odevzdá ve dvou knihařsky svázaných vyhotoveních, pokud katedra garantující studijní obor neurčí jiný počet. Vnější desky budou označeny takto:

nahoře: *Vysoká škola báňská - Technická univerzita Ostrava*

uprostřed: *DIPLOMOVÁ PRÁCE*

dole: *Rok* *Jméno a příjmení*

Kromě těchto dvou knihařsky svázaných výtisků odevzdá student kompletní práci také v elektronické formě do IS EDISON. Práce vložená v elektronické formě do IS EDISON se musí zcela shodovat s prací odevzdanou v tištěné formě. Po vložení DP do IS EDISON bude provedena její kontrola na plagiátorství.

IV.

Nesplnění výše uvedených zásad pro vypracování diplomové práce může být důvodem nepřijetí práce k obhajobě. O nepřijetí práce k obhajobě rozhoduje v tomto případě garant příslušného studijního oboru. Tyto zásady jsou závazné pro studenty navazujícího magisterského studijního programu Nanotechnologie Vysoké školy báňské – Technické univerzity Ostrava od akademického roku 2019/2020.

Ostrava 25. 11. 2019

Ing. Zdeňka Chmelíková, Ph.D.
prorektorka pro studium
VŠB-TU Ostrava

P R O H L Á Š E N Í

Prohlašuji, že

- jsem byl(a) seznámen(a) s tím, že na moji diplomovou práci se plně vztahuje zákon č. 121/2000 Sb. – autorský zákon, zejména §35 – užití díla v rámci občanských a náboženských obřadů, v rámci školních představení a užití díla školního (§60 – školní dílo);

- beru na vědomí, že Vysoká škola báňská – Technická univerzita Ostrava (dále jen VŠB – TUO) má právo nevýdělečně ke své vnitřní potřebě diplomovou práci užít (§35 odst. 3);

- souhlasím s tím, že diplomová práce bude archivována v elektronické formě v databázi Ústřední knihovny VŠB – TUO a jeden výtisk bude uložen u vedoucího diplomové práce. Souhlasím s tím, že údaje o diplomové práci budou zveřejněny v informačním systému VŠB-TUO;

- bylo sjednáno, že s VŠB – TUO, v případě zájmu z její strany, uzavřu licenční smlouvu s oprávněním užít dílo v rozsahu §12 odst. 4 autorského zákona;

- bylo sjednáno, že užít své dílo – diplomovou práci nebo poskytnout licenci k jejímu využití mohu jen se souhlasem VŠB – TUO, která je oprávněna v takovém případě ode mne požadovat přiměřený příspěvek na úhradu nákladů, které byly VŠB – TUO na vytvoření díla vynaloženy (až do jejich skutečné výše);

- beru na vědomí, že odevzdáním své diplomové práce souhlasím s jejím zveřejněním podle zákona č. 111/1998Sb., o vysokých školách a o změně a doplnění dalších zákonů (Zákon o vysokých školách) bez ohledu na výsledek její obhajoby.

Místopřísežně prohlašuji, že jsem celou diplomovou práci vypracoval(a) samostatně.

V Ostravě . . . .

podpis (jméno a příjmení studenta)

Rád bych poděkovat Ing. Dominiku Legutovi Ph.D. za odborné rady a věcné připomínky, které mi poskytl při zpracování této práce.

Abstrakt

V posledních letech vzrůstá zájem o thorium z důvodu potenciálního využití jako nukleárního paliva reaktorů IV. generace. Z důvodu jeho vysoké radioaktivity je nicméně obtížné provádět experimenty. Teoretické práce jsou tedy vysoce ceněny. Thorium disponuje pouze malým množstvím obsazených $5f$ stavů, jenž se účastní chemické vazby, a tedy vykazují itinerantní chování. Díky tomu není nutné jejich chování korigovat pomocí Hubbardova modelu. U elementů s vysokým atomovým číslem existuje však problém s popisem relativistických $6p_{1/2}$ stavů při zahrnutí spin-orbitální interakce do skalárně-relativistické kalkulace. Vliv spin-orbitální interakce je analyzován pro elektronové, elastické a fononové vlastnosti. Obdobná analýza je provedena i pro monokarbid thoria. Studie se zabývá změnami vlastností vycházející ze začlenění uhlíku do thoriové struktury. Důkladná analýza tepelné vodivosti zahrnující jak elektronový, tak i fononový příspěvek, je provedena pro Th i ThC. Zvýšená pozornost je kladena na vysvětlení, proč optické fononové větve ThC přispívají pouze 6 % z celkové fononové tepelné vodivosti. Vliv velikosti zrn a bodových defektů na fononovou tepelnou vodivost je rovněž diskutován.

Klíčová slova: ab initio, DFT, thorium, elasticita, termodynamika, fonony, jaderná paliva, tepelná vodivost, fononový rozptyl

Abstract

Thorium is beginning to attract attention because of its potential use as a nuclear fuel. It is not easy to carry out experiments because of its radioactive nature, and therefore theoretical works are highly appreciated. Thorium contains only a small number of the $5f$ states. It is generally accepted that these states are itinerant, that they form a chemical bond, and their nature does not need to be corrected with the Hubbard model. On the other hand, there is a well-known problem with the description of the $6p_{1/2}$ states when the spin-orbit coupling is added as the perturbation to a scalar-relativistic calculation. Electronic, elastic, and phonon properties are analyzed in terms of the importance of the spin-orbit coupling acting on the $6p$, $6d$, and $5f$ states. The same properties are analyzed for thorium monocarbide, and a difference caused by adding a carbon atom into the structure is discussed. Detailed analysis of the thermal conductivity (both phonon and electronic contributions) is also included. The extra attention is paid to the thermal conductivity of ThC explaining why the optical phonon modes account only for approximately 6 % of the phonon thermal conductivity. The existence of grain boundary and point defects on the phonon thermal conductivity is also discussed.

Key Words: ab initio, DFT, thorium, elasticity, thermodynamics, phonons, nuclear fuels, thermal conductivity, phonon scattering

Contents

List of Abbreviations **11**

List of Figures **12**

List of Tables **14**

1 Introduction **15**

2 Theory **16**

2.1 Hamiltonian of solid state . . . 16
2.2 Hartree approximation . . . 17
2.3 Hartree-Fock approximation . . . 17
2.4 Density Functional Theory . . . 18
2.4.1 Theorems . . . 18
2.4.2 Exchange-correlation energy . . . 19
2.4.3 Kohm-Sham equations . . . 20
2.4.4 Solution of Kohm-Sham equations . . . 20
2.4.5 Basis of Kohm-Sham orbitals . . . 21
2.4.6 Spin-orbit coupling . . . 22
2.4.7 Hubbard model . . . 24
2.5 Reciprocal lattice . . . 26
2.6 Elastic properties . . . 28
2.7 Lattice dynamics . . . 30
2.7.1 Vibration of solids . . . 30
2.7.2 Harmonic approximation . . . 30
2.8 Thermodynamics . . . 32
2.8.1 Thermodynamics within harmonic approximation at constant volume . . . 32
2.8.2 Phonon thermal conductivity . . . 33
2.8.3 Electron thermal conductivity . . . 37
2.9 Actinides . . . 40
2.9.1 5*f*-electrons and their dual nature . . . 41
2.9.2 Thorium . . . 41
2.9.3 Thorium carbides . . . 42

3 Methodology **43**

4 Results and Discussion **45**
4.1 Electronic structure of *fcc* thorium 45
4.2 Elastic properties of *fcc* thorium 47
4.3 Lattice dynamics of *fcc* thorium 48
4.4 Electronic structure of thorium monocarbide 49
4.5 Elastic properties of thorium monocarbide 50
4.6 Phonon DOS of thorium monocarbide 51
4.7 Thorium monocarbide with the Hubbard model 52
4.8 Thermal conductivity 54
4.8.1 Thermal conductivity of *fcc* thorium 54
4.8.2 Thermal conductivity of thorium monocarbide 56
4.8.3 Grain boundary 58
4.8.4 Mass-difference defects 59

5 Conclusions **61**

References **64**

List of abbreviations

APW	–	Augmented Plane Wave method
BIS	–	Bremsstrahlung Isochromat Spectroscopy
BTE	–	Boltzmann Transport Equation
DFT	–	Density Functional Theory
FLAPW	–	Full-potential Linear Augmented Plane-Wave method
GGA	–	Generalized Gradient Approximations
LA	–	Longitudinal Acoustic Mode
LAPW	–	Linearized Augmented Planewave
LDA	–	Local Density Approximation
LMTO	–	Linearized Muffin-Tin Orbital
LO	–	Longitudinal Optical Mode
PAW	–	Projector Augmented Wave
PBE	–	Perdew-Burke-Ernzerhof exchange correlation functional
PBEsol	–	Perdew-Burke-Ernzerhof exchange correlation functional for solids
RTA	–	Relaxation Time Approximation
SOC	–	Spin-Orbit Coupling
TA	–	Transverse Acoustic Mode
TO	–	Transverse Optical Mode
UPS	–	Ultraviolet Photoelectron Spectroscopy
VASP	–	Vienna Ab initio Simulation Package
XPS	–	X-ray Photoelectron Spectroscopy

List of Figures

1 Schematic chart for self-consistent density functional calculation [1]. 21
2 Schematic representation of the construction of the pseudo-wavefunction $\Psi(\boldsymbol{r})$ and pseudopotential $V^{ps}(\boldsymbol{r})$ with the cutoff radius $\boldsymbol{r}_c$ [2]. 23
3 The construction of the Wigner-Seitz cell for two-dimensional cell [3]. 27
4 The phonon thermal conductivity of a $CoSb_3$. The dots and the solid line represent the experimental data and the theoretical fit. The dashed curves are the theoretical limits [4]. 33
5 Normal (N-process) and Umklapp process (U-process) [5]. 36
6 The the *fcc* structure of Th and the rocksalt structure of ThC. 43
7 The total densities of electron states $D(E)$ for *fcc* Th with the SOC neglected and included. The filled lines represent the $6d$ (blue) and $5f$ (orange) states of the PBE model [6]. 45
8 The total electron density of states $D(E)$ of *fcc* Th for two different exchange and correlation potentials presented together with the BIS and XPS measurements [6, 7]. 46
9 The dispersion relations of *fcc* Th phonons [6]. The blue line represents PBE, the green line represents PBE+SOC($6d$,$5f$), the red line represents PBE+SOC($6p$,$6d$,$5f$), and the black squares are the experimental data [8]. 48
10 The total densities of electron states $D(E)$ for ThC [6]. 49
11 The projected densities of electron states $D(E)$ for ThC calculated with PBEsol, PBEsol+SOC($6p$,$6d$,$5f$), and PBEsol+SOC($6p$,$6d$,$5f$) with the Hubbard $U_{\text{eff}} = 3$ eV [6]. 50
12 The phonon densities of states G(E) for ThC [6]. The TOF data (circles) are taken from Wedgwood [9]. 52
13 The total densities of electron states D(E) for ThC calculated with PBEsol, PBEsol+SOC($6p$,$6d$,$5f$), and PBEsol+SOC($6p$,$6d$,$5f$) with Hubbard $U_{\text{eff}} = 3$ eV [6]. 52
14 The phonon dispersion relations and the phonon densities of states G(E) for ThC [6]. The TOF data (circles) are taken from Wedgwood [9]. 53
15 The total thermal conductivity of *fcc* Th [6]. The experimental values are from Schettler *et al.* [10] (blue and orange), Anderson *et al.* [11] (green), and March *et al.* [12] (red). 54
16 The phonon and electron parts of the thermal conductivity [6]. 55
17 The accumulated phonon thermal conductivity as a function of the phonon frequency for ThC [6]. 56
18 The phonon part and the heat capacity per mode of ThC as a function of T [6]. . 57
19 The group velocity in the xx direction and the phonon lifetime distribution of ThC as a function of the phonon frequency [6]. 57

20 The phonon thermal conductivity with a various grain sizes and the phonon mean free path of ThC (PBEsol+SOC+U_{eff}). 58
21 The phonon thermal conductivity for ThC (PBEsol+SOC+U_{eff} = 3 eV) with 10 μm grain size and defects. 60

List of Tables

1 Voigt's contraction scheme 28

2 The calculated and experimental lattice parameters (a), elastic constants c_{ij}, bulk modulus B, Sommerfeld coefficient γ, and Debye temperatures θ_D of *fcc* Th . . . 47

3 The calculated and experimental lattice parameters (a), elastic constants c_{ij}, bulk modulus B, Sommerfeld coefficient γ, and Debye temperatures θ_D of ThC 51

1 Introduction

Materials with excellent properties are needed for almost all areas of society. This creates the need to improve existing materials or find new ones with better properties. While past research was based on empirical knowledge and trial and error, current research is shifting to the design materials with usage of high-performance computing.

Theoretical research brings a greater understanding of natural laws. It provides information that is not available through an experiment. As a result, it allows us to specifically model the desired properties and thus predict more efficient materials, regardless of use. We can predict electronic, mechanical, magnetic, optical, phonon, thermodynamic, transport, and even superconducting properties of matter using quantum-mechanical calculations.

Although we are still not at the stage where we can use the most accurate theories due to computational complexity, it is already possible to obtain results in great agreement with experiments using reasonable approximations. However, higher accuracy is almost always offset by higher computational demands and the balance between accuracy and computational requirements is required.

This work deals with a novel nuclear fuel material. Nuclear fuels are a characteristic case where the usefulness of theoretical research is demonstrated. While experimenters have a difficult task to work with these materials because of high radioactivity, it is not an obstacle for theoretical research.

Theoretical investigations not only provide missing information but also predict properties under precisely defined conditions. Different stoichiometry, pressure, temperature, impurities are a solvable task for a theoretical calculation nowadays. This opens up completely new possibilities to design new materials.

The contribution of this work is based primarily on the analysis of thermal conductivity, which is very difficult to measure experimentally. The presented results can contribute to all fields where actinides or thermal conductivity is concerned.

2 Theory

2.1 Hamiltonian of solid state

An non-relativistic theory for a system of nuclei and interacting electrons is based on solving a many-body Schrödinger equation:

$$\hat{H}\Psi(\boldsymbol{r_i}, \boldsymbol{R_\alpha}) = E\Psi(\boldsymbol{r_i}, \boldsymbol{R_\alpha}), \tag{1}$$

where $\hat{H}$ is the Hamiltonian of the system and Ψ is the wavefunction of the all electron and the ion coordinates, which are labeled by $\boldsymbol{r_i}$ and $\boldsymbol{R_\alpha}$.

In most cases, we assume that the nuclei are slowly moving in space and the electrons respond instantaneously to any ionic motion. This assumption is based on the huge difference of mass between the nuclei and the electrons (3-5 orders of magnitude). It allows to treat the nuclei as static and only the wavefunction of the electrons is determined for the fixed set of the nuclei coordinates $\boldsymbol{R_\alpha}$ (Born–Oppenheimer approximation). Then the Hamiltonian of the system is:

$$\hat{H} = \sum_i \frac{\hbar^2}{2m}\nabla^2_{\boldsymbol{r_i}} + \frac{1}{2}{\sum_{i,j}}' \frac{e^2}{|\boldsymbol{r_i} - \boldsymbol{r_j}|} + \frac{1}{2}{\sum_{\alpha,\beta}}' \frac{Z_\alpha Z_\beta e^2}{|\boldsymbol{R_\alpha} - \boldsymbol{R_\beta}|} - \sum_{i,\alpha} \frac{Z_\alpha e^2}{|\boldsymbol{r_i} - \boldsymbol{R_\alpha}|}. \tag{2}$$

The first term represents the kinetic energy of the electrons. The next two terms originate from repulsive Coulomb interaction between the electrons and the nuclei. They are divided by two because interactions between i and j are the same as j and i. The last term describes the attractive Coulomb potential energy between the electrons and the nuclei.

The solution of the Schrödinger equation is an impossible task for numerous reasons. Electrons are fermions and obey the Pauli exclusion principle. It means that if two electrons of the same spin interchange position, the wavefunction Ψ must change sign, as known as the exchange property. Furthermore, each electron is affected by the motion of every other electron in the system and it results in correlation behavior.

Instead of solving the many-body system, we can use a simpler picture, in which we describe the system as a collection of classical nuclei and non-interacting quantum particles that reproduce the behavior of the real electrons. This simplified description of the electrons is called the single-particle approximation.

It is a suitable approximation when the precise knowledge of the exchange and correlation energy is not needed. For example, we can obtain classical electric conductivity but not superconductivity coming from electron correlations. However, we cannot fully neglect the exchange and correlation effects at all. We simply take them into account in an average way [2].

2.2 Hartree approximation

If we leave the many-body picture of the system, we can write the electron wavefunction from Eq. 1 as a product of wavefunctions ϕ for each single-particle i in the system:

$$\Phi^H(\{\boldsymbol{r_i}\}) = \phi_1(\boldsymbol{r}_1)\phi_2(\boldsymbol{r}_2)...\phi_n(\boldsymbol{r}_n). \tag{3}$$

The total energy of the system is then obtained by:

$$E^H = \left\langle \Psi^H | \hat{H} | \Psi^H \right\rangle = \sum_i \left\langle \Phi_i \left| \frac{-\hbar^2 \nabla_{\boldsymbol{r}}^2}{2m_e} + V_{ion}(\boldsymbol{r}) \right| \Phi_i \right\rangle + \frac{e^2}{2} \sum_{ij(j\neq i)} \left\langle \Phi_i \Phi_j \left| \frac{1}{|\boldsymbol{r} - \boldsymbol{r'}|} \right| \Phi_i \Phi_j \right\rangle. \tag{4}$$

We get the single-particle Hartree equations from Eq. 4 by using a variational argument:

$$\left[\frac{-\hbar^2 \nabla_{\boldsymbol{r}}^2}{2m_e} + V_{ion}(\boldsymbol{r}) + e^2 \sum_{j\neq i} \left\langle \Phi_j \left| \frac{1}{|\boldsymbol{r} - \boldsymbol{r'}|} \right| \Phi_j \right\rangle \right] \Phi_i(\boldsymbol{r}) = \epsilon_i \Phi_i(\boldsymbol{r}). \tag{5}$$

Each single-particle i has its effective mean-field equation which depends on other single-particle wavefunction and the problem of self-consistency has to be solved iteratively [2].

2.3 Hartree-Fock approximation

However, the Hartree approximation does not respect the fermionic nature of electrons. We need to incorporate the antisymmetry of the wavefunction to reproduce the sign change when two electrons are interchanged. It is accomplished when the wavefunction is written in a form of the Slater determinant:

$$\Phi(\{\boldsymbol{r_i}\}) = \frac{1}{\sqrt{N!}} \begin{vmatrix} \phi_1(\boldsymbol{r}_1) & \phi_2(\boldsymbol{r}_2) & \cdots & \phi_1(\boldsymbol{r}_n) \\ \phi_2(\boldsymbol{r}_1) & \phi_2(\boldsymbol{r}_2) & ... & \vdots \\ \vdots & \vdots & \ddots & \vdots \\ \phi_n(\boldsymbol{r}_1) & \cdots & \cdots & \phi_n(\boldsymbol{r}_n) \end{vmatrix}, \tag{6}$$

where N is the total number of electrons. The Slater determinant meets the antisymmetry condition because the interchange position of two electrons is equivalent to interchanging the corresponding columns in the determinant.

Including the antisymmetry of the wavefuction gives the single-particle Hartree–Fock equations:

$$\left[\frac{-\hbar^2 \nabla_{\boldsymbol{r}}^2}{2m_e} + V_{ion}(\boldsymbol{r}) + e^2 \sum_{j\neq i} \left\langle \Phi_j \left| \frac{1}{|\boldsymbol{r} - \boldsymbol{r'}|} \right| \Phi_j \right\rangle \right] \Phi_i(\boldsymbol{r}) - e^2 \sum_{j\neq i} \left\langle \Phi_j \left| \frac{1}{|\boldsymbol{r} - \boldsymbol{r'}|} \right| \Phi_i \right\rangle \Phi_j(\boldsymbol{r}) = \epsilon_i \Phi_i(\boldsymbol{r}). \tag{7}$$

The extra term represents the exchange interaction. It has a negative sign because the spatial overlap of wavefunctions with the same spin is minimized and therefore the repulsive Coulomb interaction is reduced. This reduction of the repulsive Coulomb interaction is important because it considerably increases the stability of the system. Nevertheless, the true wavefunction is not a product of the single-particles as the Hartree-Fock approximation assumes, but it is rather a complicated function of both particles simultaneously. Therefore, the correlation effects are not included in the Hartree-Fock approximation [13].

2.4 Density Functional Theory

2.4.1 Theorems

The basic concept of the Density Functional Theory (DFT) is to deal with the total density of electrons $\rho(r)$ instead of dealing with the many-body wavefunction. It is a huge simplification because the many-body wavefunction does not need to be explicitly specified as in the case of the Hartree/Hartree-Fock theory [2].

In the last two decades, the DFT has been rapidly developed and it is massively used to predict properties of matter. It finds usability in chemistry, biochemistry, physics, chemical engineering, catalysis, materials science, *etc.* The success comes from accuracy comparable with the advanced many-electron wavefunction methods but with lower computational costs [14].

Density Functional Theory is based on two theorems. The first one states that the total energy (E) of interacting electrons in an external potential (*e. g.* the Coulomb potential of nuclei) is given as a functional of the ground state electronic density ρ [1]:

$$E = E[\rho(\boldsymbol{r})]. \tag{8}$$

The second theorem states that the true electronic ground state density can be found in the minimum [1]:

$$\left.\frac{\partial E[\rho]}{\partial \rho}\right|_{\rho_0} = 0. \tag{9}$$

Unfortunately, we do not know the exact form of $E[\rho]$, and therefore the accuracy of the theory depends on sufficiently accurate approximations. It is generally accepted to express $E[\rho]$ as the sum of Hartree total energy and unknown functional, called the exchange-correlation functional:

$$E[\rho] = T_s[\rho] + E_{ei}[\rho] + E_{ii}[\rho] + E_H[\rho] + E_{xc}[\rho], \tag{10}$$

where $T_s[\rho]$ is the single particle kinetic energy, $E_{ei}[\rho]$ corresponds to the Coulomb interaction energy between the electrons and the nuclei, $E_{ii}[\rho]$ arises from the mutual interaction of the nuclei, and $E_H[\rho]$ is the Hartree component of the electron-electron energy which depends on electron density:

$$E_H[\rho] = \frac{e^2}{2} \int d^3\boldsymbol{r}\; d^3\boldsymbol{r'}\; \frac{\rho(\boldsymbol{r})\rho(\boldsymbol{r'})}{|\boldsymbol{r} - \boldsymbol{r'}|}. \tag{11}$$

The last term represents the exchange-correlation energy $E_{xc}[\rho]$.

2.4.2 Exchange-correlation energy

The exchange-correlation energy has many purposes and its exact expression is unknown. First, it should compensate for the excess repulsive Coulomb interaction which originates from neglecting the antisymmetry of the wavefunction.

The DFT treats electrons as non-interacting quantum particles. However, they interact and they are somehow correlated. These correlations are also included in the exchange-correlation energy.

The last contribution comes from the so-called self-interaction error. It originates from counting repulsive Coulomb interaction between charge density and not between electrons. As a result, the electrons interact with themselves.

The simplest expression of the exchange and correlation energy depends only on a local function of the electron density. It is called the local density approximation (LDA) and it is written as [1]:

$$E_{xc}^{LDA} = \int d^3\boldsymbol{r}\ \rho(\boldsymbol{r})\epsilon_{xc}(\rho(\boldsymbol{r})). \tag{12}$$

It works great for systems with a homogeneous electron density. We find good result for s, p, $4d$, and $5d$ metals but it fails in systems with strongly varying electron densities (*e. g.* $3d$ metals).

If we work with systems with strongly varying electron densities, we need to incorporate more information about the electron density. It leads to the generalized gradient approximation (GGA) which depends also on the local gradient of the electron density:

$$E_{xc}^{GGA} = \int d^3\boldsymbol{r}\ \rho(\boldsymbol{r})\epsilon_{xc}(\rho(\boldsymbol{r}), \Delta\rho(\boldsymbol{r})). \tag{13}$$

Including the gradient decreases the correlation energy relative to the exchange energy. The significant gradient causes that the exchange effect keeps electrons apart so that their correlation energy becomes relatively smaller [15].

There are also more advanced types of exchange-correlation functionals that incorporate even more information about the electron density. For example, the exchange-correlation energy can also depend on $\Delta^2\rho$ (metaGGA functional) or we can combine GGA functionals with non-local Hartree-Fock exchange (hybrid functional). Even though hybrid functionals are much more computationally intensive than pure GGA, they can reach the desired accuracy in many molecular properties, and they can even deliver results comparable with highly sophisticated post-HF methods [14].

2.4.3 Kohm-Sham equations

Kohm and Sham defined the electron density as a sum of single wavefunction densities obtained from the occupied single-particle Kohm-Sham orbitals $\phi_i(\boldsymbol{r})$:

$$\rho(\boldsymbol{r}) = \sum_{occ} \phi_i^*(\boldsymbol{r})\phi_i(\boldsymbol{r}). \tag{14}$$

The single-particle Kohm-Sham orbitals $\phi_i(\boldsymbol{r})$ are determined using the self-consistent solution of a set of single-particle Schrodinger-like equations (Kohm-Sham equations) with a density dependant potential:

$$\{T + V_{ei}(\boldsymbol{r}) + V_H(\boldsymbol{r}) + V_{xc}(\boldsymbol{r})\}\, \phi_i(\boldsymbol{r}) = \epsilon_i \phi_i(\boldsymbol{r}), \tag{15}$$

where T labels the single particle kinetic energy and V_{ei} corresponds to the electron-nucleus interactions. The Hartree potential V_H is defined as:

$$V_H(\boldsymbol{r}) = e^2 \int d^3\boldsymbol{r'} \frac{\rho(\boldsymbol{r'})}{|\boldsymbol{r} - \boldsymbol{r'}|}, \tag{16}$$

and the exchange-correlation potential V_{xc} is obtained from:

$$V_{ex}(\boldsymbol{r}) = \frac{\delta E_{xc}[\rho]}{\delta \rho(\boldsymbol{r})}. \tag{17}$$

Thus, instead of solving the many-body Schrodinger equation, we solve a series of single-particle equations self-consistently which is a far easier problem. Moreover, we can even simplify the solution by Bloch's theorem. The electron density has the periodicity of the lattice, so does the single-particle Kohm-Sham hamiltonian. The Kohm-Sham orbitals with different Bloch Momenta $\boldsymbol{k}$ are coupled only indirectly thought the density-dependent potential. It allows solving Kohm-Sham equations separately on a grid of sampling points in the symmetry irreducible wedge of the Brillouin zone [1].

2.4.4 Solution of Kohm-Sham equations

The DFT is classified by used representation. The choice of representation depends on the task type and the required accuracy. Although it is possible to avoid the explicit use of a basis in constructing the Kohm-Sham orbitals (*e. g.* the numerical solution of differential equations on grids), nearly all approaches rely on a basis set expansion for the Kohm-Sham equations:

$$\phi_i(\boldsymbol{r}) = \sum_{\alpha} c_{i\alpha}\phi_\alpha(\boldsymbol{r}). \tag{18}$$

The $\theta_\alpha(\boldsymbol{r})$ invokes the basis functions and the $c_{i\alpha}$ represents expansion coefficients. Since the basis functions are given, the expansion coefficients $c_{i\alpha}$ are the only variables. It means that the

total energy is variational. The solution of the self-consistent Kohm-Sham equations is found by the determination of $c_{i\alpha}$ that minimize the total energy.

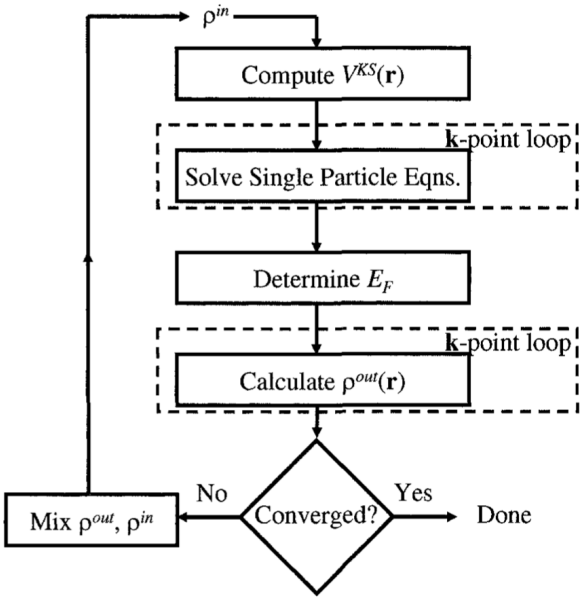

Figure 1: Schematic chart for self-consistent density functional calculation [1].

Figure 1 shows the self-consistent loop used in the DFT. It is common to separate the determination of the $c_{i\alpha}$ and the determination of the self-consistent charge density. The expansion coefficients of the single-particle equations (Eq. 15) are repeatedly determined for fixed charge density. It is mostly done using standard matrix techniques. The matrix eigenvalue equation is solved at each $\boldsymbol{k}$-point in the irreducible wedge of the Brillouin zone:

$$(\boldsymbol{H} - \epsilon_i \boldsymbol{S})\boldsymbol{c_i} = 0, \tag{19}$$

where the square matrices $\boldsymbol{H}$ and S represent the Kohm-Sham Hamiltonian and overlap matrices.

If the true occupied Kohm-Sham orbitals can be expressed as linear combinations of the basis functions, it follows that the optimization of $c_{i\alpha}$ gives the exact self-consistent solution. Therefore, a good basis is crucial for getting the total energy close to the true Kohm-Sham energy [1].

2.4.5 Basis of Kohm-Sham orbitals

There are two dominant approaches nowadays. The former employs pseudopotentials and relatively simple basis sets (particularly planewaves) and the other using methods with complex but efficient basis sets, such as the linearized augmented planewave (LAPW), the linearized muffin-tin orbital (LMTO), and related methods.

Planewave pseudopotential

Planewaves are a natural basis for a periodic crystal lattice. Bloch's theorem defines the crystal momentum $\boldsymbol{k}$, what is the conserved quantum number. It also gives the boundary condition for the single particle wavefunctions $\phi_{\boldsymbol{k}}$. Every wavefunction in a periodic potential has to satisfy the boundary condition:

$$\phi_{\boldsymbol{k}}(\boldsymbol{r} + \boldsymbol{R}_L) = e^{i\boldsymbol{k}\cdot\boldsymbol{R_L}}\phi_{\boldsymbol{k}}, \tag{20}$$

where $\boldsymbol{R_L}$ indicates the direct lattice vector. The most general solution that satisfies this boundary condition is:

$$\phi_{\boldsymbol{k}}(\boldsymbol{r}) = e^{i\boldsymbol{k}\cdot\boldsymbol{r}} \sum_{\boldsymbol{G}} c_{\boldsymbol{G}}(\boldsymbol{k}) e^{i\boldsymbol{G}\cdot\boldsymbol{r}}, \tag{21}$$

where $\boldsymbol{G}$ represent the reciprocal lattice vectors.

Planewaves are directly eigenfunctions of the kinetic energy operator ($\boldsymbol{p}^2/2m$) and Fourier transformation is simple. It is a huge advantage against other approaches. Moreover, they form a complete set. The completeness means that, at least in principle, arbitrary accuracy can be obtained by increasing the number of planewaves in the basis. It also opens the option to monitor the convergence of a calculation by varying the planewave cutoff.

On the other hand, one needs to employ a lot of planewaves to reproduce the significantly oscillating wavefunctions close to the nuclei. It makes this basis inefficient in comparison with others. However, there is a way how to avoid it. In most cases, the core electrons are strongly bound to the nuclei and they do not respond to chemical state changes. If these core states are stable to changes in the chemical environment, they can be replaced by a pseudopotential, whose the ground state wavefunction ϕ^{PS} mimics the all-electron valence wavefunction outside a selected core radius. Both the core states and the strongly oscillating parts of the valence wavefunctions are replaced, as shown in Fig. 2. It is called the frozen core approximation and the resulting pseudowavefunctions ϕ^{PS} are smooth for many elements. It allows us to employ only low $|\boldsymbol{G}|$ planewaves. But it has its price, we need to spend a huge effort to make great pseudopotentials.

The pseudopotential allows planewaves to be a simple and reasonably efficient basis. Although the frozen core approximation is generally reliable, it does not work for some elements with extended core states and the generation of the pseudopotential is difficult task [1].

2.4.6 Spin-orbit coupling

The spin-orbit coupling is a relativistic interaction of a particle's spin with its motion inside a potential. It is a correction to the scalar-relativistic approximation in order to mimic the Dirac equation. It represents a extra term in the Hamiltonian [16]:

$$\hat{H}_{SOC} = \frac{e\hbar^2}{2m_e c^2 \boldsymbol{r}} \frac{dV(\boldsymbol{r})}{d\boldsymbol{r}} \boldsymbol{S}\cdot\boldsymbol{L}, \tag{22}$$

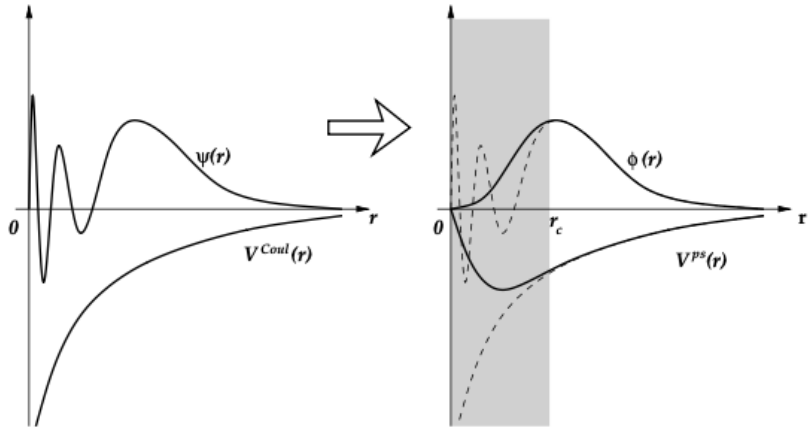

Figure 2: Schematic representation of the construction of the pseudo-wavefunction $\Psi(\boldsymbol{r})$ and pseudopotential $V^{ps}(\boldsymbol{r})$ with the cutoff radius $\boldsymbol{r}_c$ [2].

where S is the spin angular momentum and L corresponds to the orbital angular momentum.

The spin-orbit can be important for heavy elements, as well as light elements concerning properties as magneto-crystalline anisotropy, spectroscopy, and spintronics.

The spin-orbit term couples spin-up and spin-down wavefunctions and it significantly increases the robustness of the calculation. If we employ the scalar relativistic calculation with n basis functions, we need to solve $n \times n$ secular equations for each spin and $\boldsymbol{k}$-point. If we include the spin-orbit term to the Hamiltonian, we end up with $2n \times 2n$ secular equations to solve at each $\boldsymbol{k}$-point. The computation time with the size of the secular equation scales cubically. It means that including spin-orbit term causes roughly eight times bigger resource demand against the single spin scalar relativistic approximation.

However, it can be decreased. It is clear from Eq. 18 that the most efficient basis set directly consists of the Kohm-Sham orbitals or their linear combination. It cannot be used at the beginning of the calculation because the Kohm-Sham orbitals are unknown. Nevertheless, they can be used when a small perturbation ΔH (*e. g.* spin-orbit) is added to the already solved scalar-relativistic Hamiltonian. Using the low-lying Kohm-Sham orbitals of H_0 as the basis, the matrix elements with the perturbated Hamiltonian can be constructed as those of ΔH with the addition of the eigenvalues of H_0 on the diagonal. This approach is called the second variational method [1].

Although the second variational method saves a lot of computation time, it also has drawbacks. It supposes that the spin-orbit term is a small perturbation. It does not need to be true for heavy elements. Moreover, the scalar-relativistic basis can be insufficient to represent the behavior of full-relativistic orbitals. Specifically, there is a problem with the $6p_{1/2}$ basis. Unlike the $p_{3/2}$ and higher l orbitals, the $p_{1/2}$ orbital has a finite amplitude at the nucleus. It cannot be reproduced by the scalar-relativistic radial function, which for p-states goes to zero at the nucleus.

In order treat this problem, it is possible to add $l = 1$ local orbitals constructed using the full-relativistic radial function with $j = 1/2$ along with the low lying band states in the second-variational method [1].

2.4.7 Hubbard model

It is surprising that theory as the DFT can provide reasonable results for a lot of systems. We guess the correlation and exchange energy and at the same time, we deal with the self-interaction error. Predicting reasonable results is often not based on great correlation and exchange energy guesses but the mutual cancellation of errors. So it is predictable that we can found materials that the DFT fails.

Specifically, the DFT fails for atoms with partly filled d or f shells. There is generally known problem of predicting metallic ground state instead of experimentally observed insulating one for Mott insulators or uranium dioxide [17].

It can be explained by the simple frame as provided by Hubbard [18]. His theory assumes a similar rule for solids as Hund's rule for atoms. It means that there are the intra-atomic interactions that aline the electron spins on an atom with an un-filled shell.

The spin of an atom, that is the total spin of all the electrons located on that atom, fluctuates randomly in magnitude and direction due to random motion of electrons from one atom to another. The fluctuation is in an order of the electrons hopping time ($-\hbar/\Delta$ where Δ is the electron bandwidth).

An atom, which has total spin-up, attracts electrons also with spin-up and repels those with spin-down. If these intra-atomic forces are strong enough to produce appreciable correlations, the total spin of the atom may stop fluctuate and persists for a long time compared with the electron hopping time. The persistence does not come from the localization of electrons on the atom as in the case of an isolated atom. These electrons still perform their band motion but their motions are correlated in such a way to keep predominance of spin-up over spin-down on the atom. As a result, we can associate spin direction to the atom rather than electrons.

This frame clearly shows that although electrons rapidly move from atom to atom, their motions are correlated and it cannot be described by a simple model. Theoretically, the DFT would be able to cover this correlation, if the exact exchange-correlation would be known [19].

The most common approach to treating this correlation is the Hubbard model. The Hubbard model is generally made up of two terms. The first term describes the kinetic energy of the system and it is parameterized by the hopping integral t. It corresponds to the bandwidth of electronic states. The U represents the on-site repulsive interaction between two electrons, which arises from the interaction term when two electrons are placed at the same orbital site [2].

The ration between U/t determines whether the system is a insulator, semiconductor, or metal. The high value of U over t means that the electrons feel strong on-site repulsive interaction and the reduction of kinetic energy by delocalization is not preferred. As a result, they become

localized and the system is semiconductor/isolator. In the opposite case, the delocalization over lattice is preferred and the material is a metal.

The Hubbard model cannot be solved directly due to its complexity. There is a variety of approximated version. Liechtenstein, Anisimov, and Zaanen [20] approach have been chosen because it is used in a practical version of this thesis.

It assumes that the total energy $E_{tot}(n, \hat{n})$ can be written as:

$$E_{tot}(n, \hat{n}) = E_{DFT}(n) + E_{HF}(\hat{n}) - E_{dc}(\hat{n}), \tag{23}$$

where added the Hartree-Fock term $E_{HF}(\hat{n})$ describes the on-site interaction while the DFT on-site interaction is subtracted by the double counting term $E_{dc}(\hat{n})$.

The Hartree-Fock like interaction is of the form:

$$E_{HF}(\hat{n}) = \frac{1}{2} \sum_{\{\gamma\}} \left(U_{\gamma_1\gamma_2\gamma_3\gamma_4} - U_{\gamma_1\gamma_2\gamma_3\gamma_4} \right) \hat{n}_{\gamma_1\gamma_2} \hat{n}_{\gamma_3\gamma_4}. \tag{24}$$

The density matrix $\hat{n}$ are determined by the PAW on-site occupancies:

$$\hat{n}_{\gamma_1\gamma_2} = \left\langle \Psi^{s_2} | m_2 \right\rangle \left\langle m_1 | \Psi^{s_1} \right\rangle, \tag{25}$$

where $|m>$ corresponds to the real spherical harmonics of angular momentum.

The unscreened on-site electron-electron interaction $U_{\gamma_1\gamma_2\gamma_3\gamma_4}$ can be written in the terms of the Slater integrals:

$$U_{\gamma_1\gamma_2\gamma_3\gamma_4} = \sum_k a_k(m_1, m_2, m_3, m_4) F^k, \tag{26}$$

where $0 \leq k \leq 2l$ and:

$$a_k(m_1, m_2, m_3, m_4) = \frac{4\pi}{2k+1} \sum_{q=-k}^{k} \left\langle lm | Y_{kq} | lm' \right\rangle \times \left\langle lm'' | Y^*_{kq} | lm''' \right\rangle. \tag{27}$$

The Slater integrals for f electrons are $F^0 = U$, $F^2 = \frac{6435}{286+195 \cdot 0.668+250 \cdot 0.494} J$, $F^4 = 0.668F^2$, and $F^6 = 0.494F^2$.

The cancellation of dual counting is done by:

$$E_{dc}(\hat{n}) = \frac{U}{2} \hat{n}_{tot}(\hat{n}_{tot} - 1) - \frac{J}{2} \sum_{\sigma} \hat{n}^{\sigma}_{tot}(\hat{n}^{\sigma}_{tot} - 1). \tag{28}$$

Although there are some approaches on how to estimate variables U and J, it is mostly treated as a parameter which is semiempirically determined based on agreement with experimental values [19].

2.5 Reciprocal lattice

Consider a function $f(\boldsymbol{r})$ that is the same in every unit cell of a crystal, *e.g.*, electron density:

$$f(\boldsymbol{r} + \boldsymbol{T}(n_1, n_2, ..)) = f(\boldsymbol{r}), \tag{29}$$

where $\boldsymbol{T}$ is the translation vector. Any translation T can be written as integral multiples (n_i) of the primitive vectors ($\boldsymbol{a}_i$). For three dimensional case, we get:

$$\boldsymbol{T}(\boldsymbol{n}) = \boldsymbol{T}(n_1, n_2, n_3) = n_1\boldsymbol{a}_1 + n_2\boldsymbol{a}_2 + n_3\boldsymbol{a}_3. \tag{30}$$

Any periodic function can be represented by the Fourier transform in terms of the Fourier components at the wavevectors $\boldsymbol{k}$ defined in reciprocal space.

If we restrict the Fourier components to those that are periodic in a large volume of crystal Ω composed of $N_{cell} = N_1 \times N_2 \times N_3$ cells, we can simply write formulas in terms of a discrete set of the Fourier components [3].

Then each component must meet the Born-Von-Karmen periodic boundary condition:

$$e^{i\boldsymbol{k}\cdot N_1\boldsymbol{a}_1} = e^{i\boldsymbol{k}\cdot N_2\boldsymbol{a}_2} = e^{i\boldsymbol{k}\cdot N_3\boldsymbol{a}_3} = 1. \tag{31}$$

Thus, $\boldsymbol{k}$ is restricted to a set of vectors satisfying $\boldsymbol{k} \cdot \boldsymbol{a}_i = 2\pi \cdot Z$ for each of the primitive vectors $\boldsymbol{a}_i$, where Z is an integer.

The Fourier transform is defined as:

$$f(\boldsymbol{k}) = \frac{1}{\Omega}\int_{\Omega} d\boldsymbol{r}\, f(\boldsymbol{r}) e^{i\boldsymbol{k}\cdot\boldsymbol{r}} \tag{32}$$

and after substituting by the periodic function we get:

$$f(\boldsymbol{k}) = \frac{1}{\Omega}\sum_{n_1,n_2,n_2}\int_{\Omega} d\boldsymbol{r}\, f(\boldsymbol{r}) e^{i\boldsymbol{k}\cdot(\boldsymbol{r}+\boldsymbol{T}(n_1,n_2,n_3))}. \tag{33}$$

The sum over all lattice points vanishes for all $\boldsymbol{k}$ except those for which $\boldsymbol{k} \cdot \boldsymbol{T}(n_1, n_2, n_3) = 2\pi \cdot Z$ for all translations $\boldsymbol{T}$. Because the translation $\boldsymbol{T}$ is a sum of integer multiples of the primitive translations $\boldsymbol{a}_i$, it follows that $\boldsymbol{k} \cdot \boldsymbol{a}_i = 2\pi \cdot Z$.

The set of Fourier components $\boldsymbol{k}$, which satisfies this condition, represents the lattice points $\boldsymbol{G}$ of reciprocal space. In a similar way to the real lattice, we describe the translation of the reciprocal lattice:

$$\boldsymbol{G}(m_1, m_2, m_3) = m_1\boldsymbol{b}_1 + m_2\boldsymbol{b}_2 + m_3\boldsymbol{b}_3, \tag{34}$$

where m_i are integral multiples.

Since $\boldsymbol{G}$ is also the sum of integer multiples of the translations $\boldsymbol{b}_j$, we get the final formula:

$$\boldsymbol{b}_i \cdot \boldsymbol{a}_j = 2\pi\delta_{ij}, \tag{35}$$

The mutually reciprocal relation of the Bravais lattice in real space and the reciprocal lattice can be broken down as [3]:

$$\boldsymbol{b}_1 = \frac{2\pi(\boldsymbol{a}_2 \times \boldsymbol{a}_3)}{\boldsymbol{a}_1 \cdot (\boldsymbol{a}_2 \times \boldsymbol{a}_3)} \quad ; \quad b_2 = \frac{2\pi(\boldsymbol{a}_3 \times \boldsymbol{a}_1)}{\boldsymbol{a}_2 \cdot (\boldsymbol{a}_3 \times \boldsymbol{a}_1)} \quad ; \quad b_3 = \frac{2\pi(\boldsymbol{a}_1 \times \boldsymbol{a}_2)}{\boldsymbol{a}_3 \cdot (\boldsymbol{a}_1 \times \boldsymbol{a}_2)}. \tag{36}$$

Physically waves in crystals are unchanged if their wavevector is shifter by the reciprocal lattice vector $\boldsymbol{k} \rightarrow \boldsymbol{k} + \boldsymbol{G}$. It means that we can define a zone where each $\boldsymbol{k}$-point within the zone is physically different and all physically different points occur once within the zone. This zone is called the Brillouin zone [21].

For solid-state physics, band structures are only displayed in the first Brillouin zone because bands outside of the first Brillouin zone are physically equivalent to bands inside the first Brillouin zone under shifts of the wavevector $\boldsymbol{k}$ by the reciprocal lattice vector $2\pi/a$. It means that we can always express every $\boldsymbol{k}$-point outside of the first Brillouin zone within the first Brillouin zone and we do not need to show the higher Brillouin zones [21].

The first Brillouin zone is defined as the Wigner-Seitz cell of the reciprocal lattice. Therefore the construction of the first Brillouin zone is given by the planes that are the perpendicular bisectors of the vectors from the origin to the reciprocal lattice points, as shown in Fig. 3. These planes are special because the Bragg condition needed for elastic scattering is only satisfied with these planes [3].

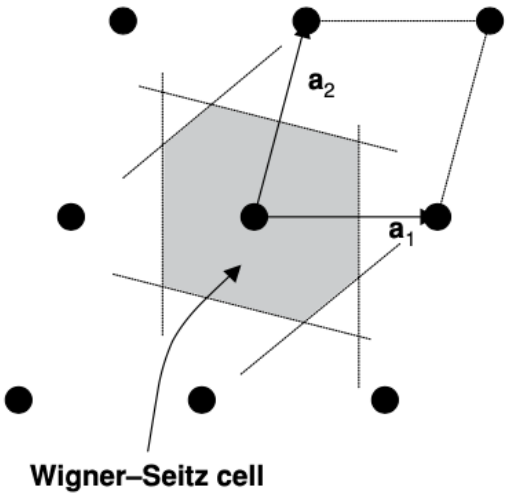

Figure 3: The construction of the Wigner-Seitz cell for two-dimensional cell [3].

2.6 Elastic properties

Hook's law, which is valid for a small perturbation, describes the relation of the elastic strain ϵ_{kl} to the stress σ_{ij}:

$$\sigma_{ij} = \sum_{k,l=1}^{3} c_{ijkl}\epsilon_{kl}, \tag{37}$$

where i, j, k, and l run from 1 to 3. Thus, the elastic properties c_{ij} of a single crystal are described by the fourth-rank elasticity tensor with 81 elements c_{ijkl}. The 81 elements are reduced to 21 elements due to the symmetry ($c_{ijkl} = c_{jkli} = c_{klij} = c_{lijk}$). Remaining 21 elements can be arranged in thesymmetric 6×6 matrix using the Voigt's contraction scheme as listed in Tab. 1.

It allows to rewrite Hook's law to a simplified form:

$$\sigma_{\alpha} = \sum_{\beta=1}^{6} c_{\alpha\beta}\epsilon_{\beta}, \tag{38}$$

where:

$$\sigma_{\alpha} = \sigma_{ij}; \qquad \epsilon_{\beta} = \epsilon_{kl} \quad if \quad \beta = 1, 2, 3; \qquad \epsilon_{\beta} = 2\epsilon_{kl} \quad if \quad \beta = 4, 5, 6 \tag{39}$$

Table 1: Voigt's contraction scheme

i, j or k, l	11	22	33	23 or 32	13 or 31	12 or 21
α or β	1	2	3	4	5	6

The number of independent elastic constants is further reduced by the crystal symmetry. For example, the most symmetric (cubic) crystal has only three independent elastic coefficients c_{11}, c_{12}, and c_{44} [22].

Hooke's law is the phenomenological description of a crystal behavior under stress. A deeper understanding including the presence of pressure or temperature is based on derivatives of thermodynamic functions.

The first law of thermodynamics states:

$$dU = TdS + pdV, \tag{40}$$

where U represents the internal energy, T invokes temperature, S is the entropy, p detonate pressure (positive stress σ corresponds to negative pressure), and V represents volume.

The second term can be reformulated in terms of stress σ_i, strain ϵ_i, and volume V_0:

$$dU = TdS + V_0 \sum_{i=1}^{6} \sigma_i d\epsilon_i. \tag{41}$$

We assume adiabatic deformation ($dS = 0$) in order to eliminate the entropic term. It means that no heat flows in or out of the volume V_0.

Then Eq. 41 can be rewritten as:

$$\sigma_i = \frac{1}{V_0}\left(\frac{\partial U}{\partial \epsilon_i}\right)_{S,\epsilon}, \tag{42}$$

where the subscripts indicate that all strains $\epsilon_j \neq \epsilon_i$ are held constant and prefactor $1/\mathrm{V}_0$ ensures that the stress σ_i is independent of the size of the specimen.

Finally, the adiabatic elastic coefficients $c_{\alpha\beta}$ are obtained:

$$(c_{\alpha\beta})_S = \left(\frac{\partial \sigma_\alpha}{\partial \epsilon_\beta}\right)_{S,\epsilon'} = \frac{1}{V_0}\left(\frac{\partial^2 U}{\partial \epsilon_\alpha \partial \epsilon_\beta}\right)_{S,\epsilon'}, \tag{43}$$

where all ϵ, except ϵ_α and ϵ_β, are kept constant.

The thermodynamic approach gives us the opportunity to simply include higher order elastic constants by expanding the internal energy U in powers of the strains ϵ_{ij}:

$$U = U(\epsilon_i = 0) + V_0 \sum c_i \epsilon_i + \frac{1}{2} V_0 \sum c_{ij} \epsilon_i \epsilon_j + \frac{1}{6} V_0 \sum c_{ijk} \epsilon_i \epsilon_j \epsilon_k + ..., \tag{44}$$

where i, j, k run from 1 to 6.

Macroscopic elastic properties can be determined from elastic coefficients. The simplest relations are found for a single crystal with cubic symmetry [22].

The bulk modulus of a cubic crystal, which represents a resistant to compressibility, can be obtained from:

$$B = \frac{c_{11} + 2c_{12}}{3}. \tag{45}$$

The Young's modulus E of a cubic crystal is defined as the ratio of uniaxial stress to strain measured along the same axis:

$$E = \frac{\sigma_1}{\epsilon_1}. \tag{46}$$

The shear stress G of a cubic crystal is defined as:

$$G = c_{44}. \tag{47}$$

2.7 Lattice dynamics

2.7.1 Vibration of solids

Although the Born-Oppenheimer approximation is suitable and useful for exploring electronic structure, it breaks down for many properties as heat capacity, thermal expansion, thermal conductivity, infrared absorption, *etc.*

Atoms in solids vibrate around their equilibrium position with an amplitude which depends on temperature. These vibrations are not independent as assume the Einstein model. To obtain agreement with experiments, we have to consider thermal vibrations as the collective motion of atoms.

These collective motions are called phonons. They are bosons so do not obey the Pauli exclusion principle. They follow Bose-Einstein statistics and their population vastly differs from electrons.

In order to describe lattice dynamics, we define a displacement from the equilibrium position $\boldsymbol{u}$ as the difference between the current position of the atomic nuclei $\boldsymbol{R}$ and the equilibrium positions of the atomic nuclei as $\boldsymbol{R_0}$:

$$\boldsymbol{u} = \boldsymbol{R} - \boldsymbol{R}_0. \tag{48}$$

Then the Hamiltonian of an ion can be written as the expansion [23]:

$$\mathcal{H} = \Phi_0 + \mathcal{T} + \mathcal{V}_2 + \mathcal{V}_3 + ..., \tag{49}$$

with

$$\mathcal{T} = \frac{1}{2}\sum_{l\kappa\alpha} M_\kappa \left(\frac{\partial \nu}{\partial u_\alpha(l\kappa)}\right)^2, \tag{50}$$

$$\mathcal{V}_2 = \frac{1}{2}\sum_{l\kappa\alpha}\sum_{l'\kappa'\beta} \frac{\partial^2 \nu}{\partial u_\alpha(l\kappa)\partial u_\beta(l'\kappa')}\ u_\alpha(l\kappa)u_\beta(l'\kappa'), \tag{51}$$

$$\mathcal{V}_3 = \frac{1}{6}\sum_{l\kappa\alpha}\sum_{l'\kappa'\beta}\sum_{l''\kappa''\gamma} \frac{\partial^3 \nu}{\partial u_\alpha(l\kappa)\partial u_\beta(l'\kappa')\partial u_\gamma(l''\kappa'')} \times u_\alpha(l\kappa)u_\beta(l'\kappa')u_\gamma(l''\kappa''), \tag{52}$$

where Φ_0, $\mathcal{T}$, and $\mathcal{V}_n$ represent the constant potential, kinetic energy, and n-body crystal potential terms for κ-th atom in l-th unit cell. Indexes α, β, γ correspond to the Cartesian indices. The ν represents the total potential governing the ionic motion and M_κ detonates the atomic mass of κ-th atom.

2.7.2 Harmonic approximation

It is sufficient to approximate the Hamiltonian of the system (Eq. 49) only up to the quadratic term for most materials at temperature well below the melting point. It is convenient because

the solution is much simpler compared to one including higher terms. It yields:

$$\mathcal{H} = \Phi_0 + \frac{1}{2}\sum_{l\kappa\alpha} M_\kappa \left(\frac{\partial \nu}{\partial u_\alpha(l\kappa)}\right)^2 + \frac{1}{2}\sum_{l\kappa\alpha}\sum_{l'\kappa'\beta} \phi_{\alpha\beta}(l\kappa, l'\kappa')\ u_\alpha(l\kappa)u_\beta(l'\kappa'). \tag{53}$$

where $\phi_{\alpha\beta}(l\kappa)$ is called the second-order force-constant matrix and it is proportional to the force generated on the atom κ', when the atom κ is displaced by in the direction α [24]:

$$\phi_{\alpha\beta}(l\kappa, l'\kappa') = \frac{\partial^2 \nu}{\partial u_\alpha(l\kappa)\partial u_\beta(l'\kappa')}. \tag{54}$$

If the system is not exposed by external forces, the translational and rotational invariance conditions reduce the number of independent elements in the matrix. For example, the translational invariance yields [24]:

$$\sum_m \phi_{\alpha\beta}(l\kappa, l'\kappa') = 0, \tag{55}$$

which is also a consequence of third law of motion.

The translational symmetry of the force constants is a key property. It allows to write displacements in the form of planewaves:

$$\boldsymbol{u}(l\kappa) = u_{0\kappa}(\boldsymbol{q}, \nu)e^{i(\boldsymbol{q}\cdot\boldsymbol{R}(l\kappa) - \omega(\boldsymbol{q},\nu)t)}, \tag{56}$$

where $\boldsymbol{q}$ is the wavevector, ω represents frequency, and ν labels the mode.

It means that the displacement of the κ ion in the l primitive cell is related to the displacement of the corresponding ion κ in the primitive cell ($l = 0$). Every planewave has assigned the wavevector $\boldsymbol{q}$ and frequency ω.

The equation of motion of the κ-th atom from the classical Newton equation is defined:

$$M_\kappa \frac{\partial^2 \boldsymbol{u}(l\kappa)}{\partial t^2} = -\frac{\partial \mathcal{V}_2}{\partial \boldsymbol{u}(l\kappa)}. \tag{57}$$

Using Eqs. 51 and 56, we get:

$$M_\kappa \omega^2 \boldsymbol{u}_{0\kappa}(\boldsymbol{q}, \nu) = \sum_{l'\kappa'} \phi(0\kappa, l'\kappa')\boldsymbol{u}_{l'\kappa'}(\boldsymbol{q}, \nu)\ e^{-i\boldsymbol{q}\cdot(\boldsymbol{R}(l'\kappa') - \boldsymbol{R}(0\kappa))}\ , \tag{58}$$

for the κ iont in zero primitive cell. The equations of motion for a single solution (labeled ν) can be written in a vector form:

$$\boldsymbol{D}_{kk'}(\boldsymbol{q})\,\boldsymbol{e}(\boldsymbol{q}, \nu) = \omega^2(\boldsymbol{q}, \nu)\boldsymbol{e}(\boldsymbol{q}, \nu), \tag{59}$$

where the column vector $\boldsymbol{e}(\boldsymbol{q}, \nu)$ is composed of the displacement vector weighted by the square root of the atomic mass. It gives $3n$ elements at total where n represents the number of atoms per unit cell [25].

Dynamic properties in the harmonic approximation are obtained by solving the eigenvalue problem of the dynamic matrix $D_{kk'}(\boldsymbol{q})$. Since $\boldsymbol{D}_{kk'}(\boldsymbol{q})$ is a Hermitian matrix, its eigenvalues (ω^2) are real. Imaginary eigenvalues (negative frequencies) corresponds to crystal instability. The dynamic matrix $D_{kk'}(\boldsymbol{q})$ has a form:

$$\boldsymbol{D}_{kk'}(\boldsymbol{q}) = \sum_{l'} \frac{\phi(k0, k'l')\ e^{-i\boldsymbol{q}\cdot(\boldsymbol{R}(l'\kappa')-\boldsymbol{R}(0\kappa))}}{\sqrt{M_k M'_k}}. \tag{60}$$

2.8 Thermodynamics

The solving of the eigenvalue problem (Eq. 59) results in the phonon dispersion relation, *i. e.* the dependency of frequency ω on the wave vector $\boldsymbol{q}$.

It allows us to find out the group velocity of the phonon mode $\boldsymbol{q}$:

$$v_{\boldsymbol{g}} = \frac{\partial \omega}{\partial \boldsymbol{q}} \tag{61}$$

and thermodynamic properties within the harmonic approximation.

2.8.1 Thermodynamics within harmonic approximation at constant volume

The energy E of the phonon system can be obtained by summation over the first Brillouin zone and phonon modes with the use of Bose-Einstein statistics:

$$E = \sum_{\boldsymbol{q}\nu} \hbar\omega(\boldsymbol{q}\nu) \left[\frac{1}{2} + \frac{1}{e^{(\hbar\omega)/(k_B T)} - 1}\right], \tag{62}$$

where T is temperature and the constant $\frac{1}{2}$ corresponds to the zero-point energy of a quantum harmonic oscillator.

There is not way how to measure the total energy of a phonon system. A substantially useful property is heat capacity, which can be directly measured and compared with theory if the volume is kept constant [23]:

$$C_V = \left(\frac{\partial E}{\partial T}\right) = \sum_{\boldsymbol{q}m} C_{\boldsymbol{q}m} = \sum_{\boldsymbol{q}m} k_B \left(\frac{\hbar\omega_{\boldsymbol{q}m}}{k_B T}\right)^2 \frac{e^{(\hbar\omega_{\boldsymbol{q}m})/(k_B T)}}{[e^{(\hbar\omega_{\boldsymbol{q}m})/(k_B T)} - 1]^2}. \tag{63}$$

For theoretical purposes, the Helmholtz free energy F_{ph} represents important property which is needed mainly for the determination of phase stability [23]:

$$F_{ph} = \frac{1}{2}\sum_{\boldsymbol{q}m} \hbar\omega_{\boldsymbol{q}m} + k_B T \sum_{\boldsymbol{q}m} ln\left[1 - e^{-(\hbar\omega_{\boldsymbol{q}m})/(k_B T)}\right]. \tag{64}$$

Finally, the entropy S is easily derived from the Helmholtz free energy F_{ph} [23]:

$$S = -\frac{\partial F}{\partial T} = \frac{1}{2T}\sum_{\boldsymbol{q}m}\hbar\omega_{\boldsymbol{q}m}coth\frac{\hbar\omega_{\boldsymbol{q}m}}{2k_BT} - k_B\sum_{\boldsymbol{q}m} ln\left[2sinh\frac{\hbar\omega_{\boldsymbol{q}m}}{2k_BT}\right]. \tag{65}$$

2.8.2 Phonon thermal conductivity

Harmonic phonons do not scatter and their lifetimes are infinite. Such lifetimes imply that phonon heat would propagate at group velocity from one place to another without any scattering and the thermal equilibrium of the system cannot be reached. Phonon scattering is needed for the correct description of lattice dynamics.

There are many sources of scattering, *i. e.* defects, grain boundaries, isotope varying, electron-phonon, and phonon-phonon interactions. All have different importance for various materials and temperatures. The dashed lines in Fig. 4 correspond to the theoretical limits on the phonon thermal conductivity by grain boundary scattering, by a combination of boundary plus point-defect scattering, and by phonon-phonon (Umklapp) scattering for $CoSb_3$. While grain boundary and defect scatterings prevail at low temperatures, phonon-phonon scattering dominates around room temperature and above. It means that phonon-phonon scattering is the most important among others for high-temperature operations of nuclear fuels.

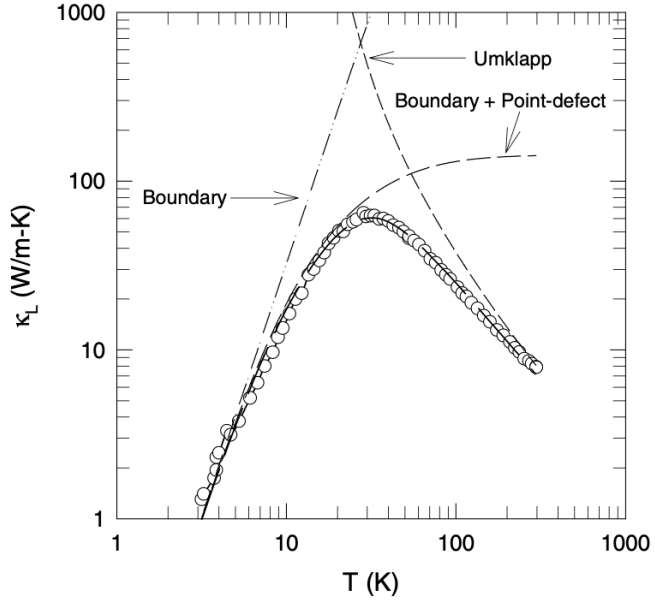

Figure 4: The phonon thermal conductivity of a $CoSb_3$. The dots and the solid line represent the experimental data and the theoretical fit. The dashed curves are the theoretical limits [4].

Phonons are bosons and obey the Bose-Einstein distribution function. The equilibrium distribution is described as:

$$n^0_{\boldsymbol{q}}(\omega, T) = \frac{1}{e^{\hbar\omega_{\boldsymbol{q}}/k_BT} - 1}, \tag{66}$$

where k_B is the Boltzmann constant [26].

When the system is perturbed, the phonon distribution changes and inhomogeneities and temporal evolution appear. The evolution of the distribution function can be described by the Boltzmann Transport Equation (BTE), which was originally introduced by Boltzmann in 1892. Instead of the equilibrium distribution, the nonequilibrium distribution function $f(\boldsymbol{r}, \boldsymbol{k}, t)$ is used to describe the system at time t in a unit volume near the point $\boldsymbol{r}$ and have the wave vector $\boldsymbol{k}$.

The evolution in time depends on diffusion process associated with temperature (concentration) gradient [26]:

$$\frac{\partial f}{\partial t} = \frac{\partial f}{\partial t}\Big|_{diff} + \frac{\partial f}{\partial t}\bigg|_{field} + \frac{\partial f}{\partial t}\bigg|_{scatt}. \tag{67}$$

Phonons cannot be affected by external fields, so $\frac{\partial n}{\partial t}|_{field}$ equals zero. The diffusion term in the presence of temperature is [27]:

$$\frac{\partial n_{\boldsymbol{q}}}{\partial t}\bigg|_{diff} = \boldsymbol{v_g}\frac{\partial n_{\boldsymbol{q}}}{\partial r}, \tag{68}$$

where $\boldsymbol{v_g}$ represents the phonon group velocity.

The scattering term depends on the number of scattering sources. We take into account only the phonon-phonon scattering due to the predominant nature at high temperature. Other terms can be added later.

The scattering term includes products of the distribution function of phonons involved in the collision. We need at least three phonon collision for phonon thermal conductivity. Then the scattering term has the form [27]:

$$\frac{\partial n_{\boldsymbol{q}}}{\partial t}\bigg|_{scattering} = \int\int [n_{\boldsymbol{q}} n_{\boldsymbol{q'}}(n_{\boldsymbol{q''}}+1) - \frac{1}{2} n_{\boldsymbol{q}}(n_{\boldsymbol{q'}}+1)(n_{\boldsymbol{q'}}+1)]\Omega_{\boldsymbol{q},\boldsymbol{q'},\boldsymbol{q''}}\frac{d\boldsymbol{q'}d\boldsymbol{q''}}{(2\pi)^3}, \tag{69}$$

where $\Omega_{\boldsymbol{q},\boldsymbol{q'},\boldsymbol{q''}}$ is the transition probability of the collision of two phonon $\boldsymbol{q}$ and $\boldsymbol{q'}$ to the outgoing phonon $\boldsymbol{q''}$.

The final form of the BTE for three phonon scattering in temperature gradient gives:

$$\frac{\partial n_{\boldsymbol{q}}}{\partial t} + \boldsymbol{v_g}\frac{\partial n_{\boldsymbol{q}}}{\partial r} = \int\int [n_{\boldsymbol{q}} n_{\boldsymbol{q'}}(n_{\boldsymbol{q''}}+1) - \frac{1}{2} n_{\boldsymbol{q}}(n_{\boldsymbol{q'}}+1)(n_{\boldsymbol{q'}}+1)]\Omega_{\boldsymbol{q},\boldsymbol{q'},\boldsymbol{q''}}\frac{d\boldsymbol{q'}d\boldsymbol{q''}}{(2\pi)^3}. \tag{70}$$

The left side of Eq. 70 is diagonal and easily solved. The complexity of the BTE comes from the scattering term. The scattering term makes the BTE a non-linear integro-differential equation that cannot be solved analytically and approximations have to be done.

The first approximation is to transform Eq. 70 to a linear equation. It is made by the linearization of a perturbation. Then the distribution function can be expressed as the equilibrium

term and a deviation from it:

$$n_{\boldsymbol{q}} = n^0_{\boldsymbol{q}} + \delta n_{\boldsymbol{q}}, \tag{71}$$

where the general perturbation A from equilibrium (in the simplest case just temperature T) can be written as [26]:

$$\delta n_{\boldsymbol{q}} = \frac{\partial n_{\boldsymbol{q}}}{\partial \epsilon_{\boldsymbol{q}}} \frac{\partial \epsilon_{\boldsymbol{q}}}{\partial A} \nabla A \cdot \Delta \boldsymbol{r} = \frac{\partial n_{\boldsymbol{q}}}{\partial \epsilon_{\boldsymbol{q}}} \Phi_{\boldsymbol{q}} = \frac{n^0_{\boldsymbol{q}}(n^0_{\boldsymbol{q}} + 1)}{k_B T} \Phi_{\boldsymbol{q}}, \tag{72}$$

Combining Eqs. 69, 71, and 72, we get the simplified version of the scattering term [26]:

$$\left.\frac{\partial n_{\boldsymbol{q}}}{\partial t}\right|_{scattering} = \int\int [\Phi_{\boldsymbol{q}} - \Phi_{\boldsymbol{q'}} - \Phi_{\boldsymbol{q''}}] P_{\boldsymbol{q},\boldsymbol{q'},\boldsymbol{q''}} \frac{d\boldsymbol{q'} d\boldsymbol{q''}}{(2\pi)^3}, \tag{73}$$

where $P_{\boldsymbol{q},\boldsymbol{q'},\boldsymbol{q''}}$ corresponds to the equilibrium transition rate. The BTE modified in this way is called the linearized BTE (LBTE).

The linearization enormously simplify the scattering term. It allows us to express the LBTE in an operator form:

$$\boldsymbol{Dn} = \boldsymbol{Cn}, \tag{74}$$

where D and C are the drift and scattering operators. The linearization allows us inverting the operators and obtaining eigenstates and eigenfunctions:

$$\boldsymbol{n} = \boldsymbol{D^{-1}Cn} = \boldsymbol{C^{-1}Dn}. \tag{75}$$

This approximation is still not enough to find an analytical solution due to the non-diagonal form of the scattering term and huge number of modes in the system. The modification to diagonal form can be done by the Relaxation Time Approximation (RTA). The RTA assumes that the rate at which the phonon $\boldsymbol{q}$ relaxes does not depend on the non-equilibrium situation of the phonons with which it interacts. It means that two phonons are consider to be in the equilibrium ($n_{\boldsymbol{q'}} = n^0_{\boldsymbol{q'}}; n_{\boldsymbol{q''}} n_{\boldsymbol{q}} = n^0_{\boldsymbol{q''}}$ and only the third one is out of equilibrium $n_{\boldsymbol{q}} = n^0_{\boldsymbol{q}} + \Delta n_{\boldsymbol{q}}$. This assumption gives the diagonal BTE [26]:

$$v_{\boldsymbol{q}} \nabla n^0_{\boldsymbol{q}} = -\frac{n_{\boldsymbol{q}} - n^0_{\boldsymbol{q}}}{\tau_{\boldsymbol{q}}}, \tag{76}$$

where $\tau_{\boldsymbol{q}}$ is the relaxation time of the phonon mode $\boldsymbol{q}$:

$$\frac{1}{\tau_{\boldsymbol{q}}} = \Phi_{\boldsymbol{q}} \int\int P_{\boldsymbol{q},\boldsymbol{q'},\boldsymbol{q''}} \frac{d\boldsymbol{q'} d\boldsymbol{q''}}{(2\pi)^3}. \tag{77}$$

Eq. 76 implies that the distribution function relaxes to the equilibrium by $\delta n_{\boldsymbol{q}}(t)(t_0)e^{-t/\tau}$ when a phonon is excited. The relaxation time τ is independent of the rest of the distribution.

Finally, we get the linear solution [26]:

$$n_{\boldsymbol{q}} = n^0_{\boldsymbol{q}} + \tau_{\boldsymbol{q}} v_{\boldsymbol{q}} \nabla n_{\boldsymbol{q}}. \tag{78}$$

However, Eq. 77 for the relaxation time does not respect the energy and momentum conservation. It follows that all scattering between phonon modes are allowed and able to relax the distribution function to the equilibrium. This is not true because only scattering satisfying the conservation laws can happen [26]. Instead of using Eq. 77, we utilize the approach analogous to Fermi's golden rule to get the relaxation times satisfying conservation laws [28].

First, the scattering of three phonons is determined [28]:

$$\Phi_{\lambda\lambda'\lambda''} = \frac{1}{\sqrt{N}} \frac{1}{3!} \sum_{\kappa\kappa'\kappa''} \sum_{\alpha\beta\gamma} W_\alpha(\kappa,\lambda) W_\beta(\kappa',\lambda') W_\gamma(\kappa'',\lambda'') \sqrt{\frac{\hbar}{2m_\kappa \omega_\lambda}} \sqrt{\frac{\hbar}{2m'_\kappa \omega_{\lambda'}}} \sqrt{\frac{\hbar}{2m''_\kappa \omega_{\lambda''}}} \tag{79}$$

$$\times \sum_{l'l''} \Phi_{\alpha\beta\gamma}(0\kappa, l'\kappa', l''\kappa'') e^{i\boldsymbol{q}'\cdot[\boldsymbol{r}(l'k')-\boldsymbol{r}(0\kappa)]} e^{i\boldsymbol{q}''\cdot[\boldsymbol{r}(l''k'')-\boldsymbol{r}(0\kappa)]} e^{i\boldsymbol{q}'''\cdot[\boldsymbol{r}(l'''k''')-\boldsymbol{r}(0\kappa)]} \Delta(\boldsymbol{q}+\boldsymbol{q}'-\boldsymbol{q}''),$$

where λ is a abbreviation for $(\boldsymbol{q}, j)$. The last term equals one only if the crystal momentum conservation law is fulfilled [29]:

$$\boldsymbol{q} + \boldsymbol{q}' = \boldsymbol{q}'' + \boldsymbol{G}. \tag{80}$$

If $\boldsymbol{G}$ equals to zero, the scattering is called Normal. Non-zero $\boldsymbol{G}$ refers to the Umklapp process. Both types of scattering are shown in Fig. 5. The Umklapp processes limit phonon thermal conductivity considerably more than Normal processes because the Umklapp process changes the net flow of heat into the opposite direction while the Normal scattering preserves the net flow in the direction [25].

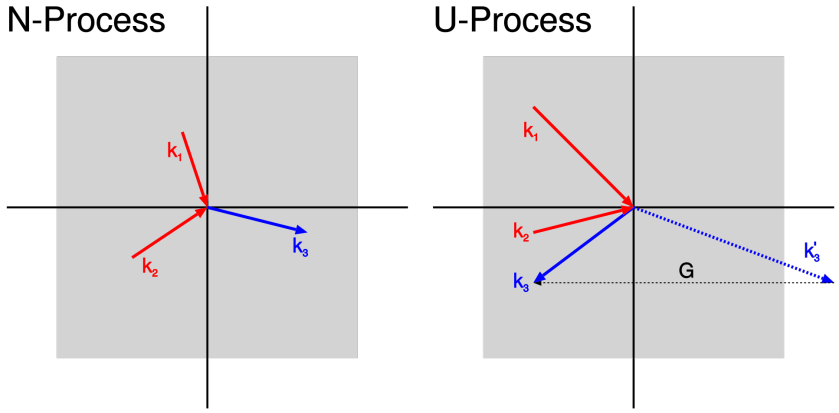

Figure 5: Normal (N-process) and Umklapp process (U-process) [5].

The imaginary part of the self-energy $\Gamma_\lambda(\omega)$ is determined from the scaterring $\Phi_{\lambda\lambda'\lambda''}$ [28]:

$$\Gamma_\lambda(\omega) = \frac{18\pi}{\hbar^2} \sum_{\lambda'\lambda''} |\Phi_{-\lambda\lambda'\lambda''}|^2 \{(n_{\lambda'} + n_{\lambda''} + 1)\delta(\omega - \omega_{\lambda'} - \omega_{\lambda''}) \tag{81}$$

$$+(n_{\lambda'} - n_{\lambda''})\left[\delta(\omega + \omega_{\lambda'} - \omega_{\lambda''}) - \delta(\omega - \omega_{\lambda'} + \omega_{\lambda''})\right]\}.$$

The $\delta(\omega - \omega_{\lambda'} + \omega_{\lambda''})$ ensures the conservation law of energy. Two times multiplied $\Gamma_\lambda(\omega)$ corresponds to the phonon linewidth and the relaxation time is obtained as an inverse value:

$$\tau_{\boldsymbol{q}}\nu) = \frac{1}{2\Gamma_{\boldsymbol{q}\nu}(\omega_{\boldsymbol{q}\nu})}. \tag{82}$$

Finally, the phonon thermal conductivity can be expressed from Eq. 77 using the microscopic definition of the heat flux $\boldsymbol{Q} = \langle \hbar\omega v_{\boldsymbol{q}} \rangle$ and Fourier law $\boldsymbol{Q} = -\kappa\nabla T$ [26]:

$$\kappa^{ij} = \int \hbar v_\lambda^i v_\lambda^j \tau_\lambda \frac{\partial n_\lambda^0(\omega)}{\partial T} D(\omega) d\omega, \tag{83}$$

where $D(\omega)$ indicates the phonon density of states and $\hbar\omega\frac{\partial n_\lambda^0(\omega)}{\partial T}$ is the mode specific heat.

For finite number of $\boldsymbol{q}$ points, we get:

$$\kappa^{ij} = \sum_\lambda C_\lambda v_\lambda^i v_\lambda^j \tau_\lambda. \tag{84}$$

2.8.3 Electron thermal conductivity

This section was inspired by Ref. [27].

The electron transport properties can be also obtained from the BTE with some changes. Electrons are not bosons as phonons but fermions. They obey the Fermi-Dirac distribution which is valid only for the equilibrium state:

$$f^0(\boldsymbol{k}, T) = \frac{1}{1 + e^{\frac{\epsilon(\boldsymbol{k}) - \mu}{k_B T}}}, \tag{85}$$

where $\epsilon(\boldsymbol{k})$ is the energy of the $\boldsymbol{k}$ point and μ accounts for the chemical potential.

To describe the non-equilibrium distribution function, we also start from the general BTE (Eq. 70) corresponding to the distribution of the perturbated system. The diffusion term is same as for phonons:

$$\left.\frac{\partial f_{\boldsymbol{k}}}{\partial t}\right|_{diff} = \boldsymbol{v}_{\boldsymbol{k}} \frac{\partial f_{\boldsymbol{k}}}{\partial r}, \tag{86}$$

where $\boldsymbol{v}_{\boldsymbol{k}}$ represents the group velocity of electrons. The first difference compared to phonons is the external field term, which can be non-zero for electrons. Although the external field term is not needed for the electron thermal conductivity, the stationary electrical field $\boldsymbol{E}$ is added to obtain the electrical conductivity:

$$\left.\frac{\partial f_{\boldsymbol{k}}}{\partial t}\right| = -\frac{e}{\hbar}\boldsymbol{E}\frac{\partial f_{\boldsymbol{k}}}{\partial k}. \tag{87}$$

All terms put together with the scattering term give the Boltzmann transport equation for electrons in the stationary electrical field and temperature gradient:

$$\boldsymbol{v_k}\frac{\partial f_{\boldsymbol{k}}}{\partial r} - \frac{e}{\hbar}\boldsymbol{E}\frac{\partial f_{\boldsymbol{k}}}{\partial k} = \left.\frac{\partial f_{\boldsymbol{k}}}{\partial t}\right|_{scatt}. \tag{88}$$

The scattering term makes finding solution complicated. Every possible transition from the $\boldsymbol{k}$ to $\boldsymbol{k'}$ state has to be considered due to defects, electron-electron, and electron-phonon interaction. Moreover, electrons are fermions and the Pauli's exclusion principle has to be taken into account. The transition from the $\boldsymbol{k}$ state (with probability f($\boldsymbol{k}$)) can take place only to the $\boldsymbol{k'}$ state if the $\boldsymbol{k'}$ state is vacant (1-f($\boldsymbol{k'}$)):

$$\int \frac{d\boldsymbol{k'}}{(2\pi)^3} W_{\boldsymbol{kk'}} f(\boldsymbol{k})(1 - f(\boldsymbol{k'})), \tag{89}$$

where $W_{\boldsymbol{kk'}}$ is the per-unit-time probability of electron transition from the $\boldsymbol{k}$ to $\boldsymbol{k'}$ state.

The same transition has to be considered for the transition $\boldsymbol{k'}$ to $\boldsymbol{k}$:

$$\int \frac{d\boldsymbol{k'}}{(2\pi)^3} W_{\boldsymbol{kk'}} f(\boldsymbol{k'})(1 - f(\boldsymbol{k})). \tag{90}$$

The difference between the number of excitation and deexcitation gives the variation rate of the nonequilibrium distribution function:

$$\left.\frac{\partial f}{\partial t}\right|_{scatt} = \int \frac{d\boldsymbol{k'}}{(2\pi)^3} \left[W_{\boldsymbol{kk'}} f(\boldsymbol{k})(1 - f(\boldsymbol{k'})) - W_{\boldsymbol{kk'}} f(\boldsymbol{k'})(1 - f(\boldsymbol{k}))\right]. \tag{91}$$

Because the resulting non-linear integro-differential equation cannot be easily solved, we need to introduce an approximation. We already know from the phonon BTE that it can be achieved by the relaxation time approximation (RTA). We assume only a linear perturbation $\delta f(\boldsymbol{r}, \boldsymbol{k})$ originated from external electrical field and temperature gradient:

$$f(\boldsymbol{r}, \boldsymbol{k}, t) = f_0(\boldsymbol{r}, \boldsymbol{k}) + \delta f(\boldsymbol{r}, \boldsymbol{k}), \tag{92}$$

where $f_0(\boldsymbol{r}, \boldsymbol{k})$ corresponds to the local equilibrium function:

$$f^0(\boldsymbol{r}, \boldsymbol{k}) = \frac{1}{1 + e^{\frac{\epsilon(\boldsymbol{k}) - \mu(\boldsymbol{r})}{k_B T}}}, \tag{93}$$

with the local chemical potential $\mu(\boldsymbol{r})$. The deviation from equilibrium is small in most cases:

$$|\delta f| = |f - f_0| \ll f_0. \tag{94}$$

If we assume that $W_{\boldsymbol{k},\boldsymbol{k'}}$ does not depend on external electric field or temperature gradient,

we get $W_{\boldsymbol{k},\boldsymbol{k'}}$ same for both equilibrium and nonequilibrium. In the equilibrium, the number of electrons coming into the $\boldsymbol{k}$ state from $\boldsymbol{k'}$ state has to be equal to the number of electrons coming out from the $\boldsymbol{k}$ into the $\boldsymbol{k'}$:

$$W_{\boldsymbol{k}\boldsymbol{k'}} f(\boldsymbol{k})(1 - f(\boldsymbol{k'})) = W_{\boldsymbol{k}\boldsymbol{k'}} f(\boldsymbol{k'})(1 - f(\boldsymbol{k})). \tag{95}$$

Substituting Eq. 92 into Eq. 91 using Eq. 94 and 95, we get:

$$\left.\frac{\partial f}{\partial t}\right|_{scatt} = \frac{\delta f(\boldsymbol{k})}{\tau(\boldsymbol{k})}, \tag{96}$$

where the relaxation time $\tau(\boldsymbol{k})$ characterizes the recovery speed of the equilibrium state and is defined as:

$$\frac{1}{\tau(\boldsymbol{k})} = \int \frac{d\boldsymbol{k'}}{(2\pi)^3} W_{\boldsymbol{k}\boldsymbol{k'}} \left(\frac{1 - f_0(\boldsymbol{k'})}{1 - f_0(\boldsymbol{k})} - \frac{f_0(\boldsymbol{k})}{f_0(\boldsymbol{k'})} \frac{\delta f(\boldsymbol{k'})}{\delta f(\boldsymbol{k})} \right). \tag{97}$$

It gives us the BTE for electrons in the stationary electric field and temperature gradient:

$$\boldsymbol{v}_{\boldsymbol{k}} \frac{\partial f(\boldsymbol{r},\boldsymbol{k})}{\partial r} - \frac{e}{\hbar} \boldsymbol{E} \frac{\partial f(\boldsymbol{r},\boldsymbol{k})}{\partial \boldsymbol{k})} = \frac{f(\boldsymbol{r},\boldsymbol{k}) - f_0(\boldsymbol{r},\boldsymbol{k})}{\tau(\boldsymbol{k})}. \tag{98}$$

Assuming $\delta f \ll f(\boldsymbol{r},\boldsymbol{k})$, the partial derivation of the local time-dependent equilibrium function $f(\boldsymbol{r},\boldsymbol{k},t)$ can be replaced by the partial derivation of the local equilibrium function $f(\boldsymbol{r},\boldsymbol{k})$.

It allows us to express partial derivations:

$$\frac{\partial f(\boldsymbol{r},\boldsymbol{k})}{\partial \boldsymbol{r}} = \left[\frac{\partial \mu}{\partial \boldsymbol{r}} + \frac{\epsilon(\boldsymbol{k}) - \mu(\boldsymbol{r})}{T} \frac{\partial T}{\partial \boldsymbol{r}} \right] \left(-\frac{\partial f_0(\boldsymbol{r},\boldsymbol{k})}{\partial \epsilon} \right), \tag{99}$$

$$\frac{\partial f(\boldsymbol{r},\boldsymbol{k})}{\partial \boldsymbol{k}} = \hbar \boldsymbol{v} \frac{\partial f_0(\boldsymbol{r},\boldsymbol{k})}{\partial \epsilon}. \tag{100}$$

Substituting Eqs. 99 and 100 into Eq. 98, it comes:

$$f(\boldsymbol{r},\boldsymbol{k}) = f_0(\boldsymbol{r},\boldsymbol{k}) - \tau(\boldsymbol{k}) \boldsymbol{v}(\boldsymbol{k}) \left[e\boldsymbol{E} + \frac{\epsilon(\boldsymbol{k}) - \mu(\boldsymbol{r})}{T} \frac{\partial}{\partial \boldsymbol{r}} T \right] \left(-\frac{\partial f_0(\boldsymbol{r},\boldsymbol{k})}{\partial \epsilon} \right), \tag{101}$$

$$\delta f(\boldsymbol{r},\boldsymbol{k}) = -\tau(\boldsymbol{k}) \boldsymbol{v}(\boldsymbol{k}) \left[e\boldsymbol{E} + \frac{\epsilon(\boldsymbol{k}) - \mu(\boldsymbol{r})}{T} \frac{\partial}{\partial \boldsymbol{r}} T \right] \left(-\frac{\partial f_0(\boldsymbol{r},\boldsymbol{k})}{\partial \epsilon} \right). \tag{102}$$

The electron current density $j_\alpha(\boldsymbol{r})$ in reciprocal space is defined as:

$$j_\alpha(\boldsymbol{r}) = -\frac{2e}{(2\pi)^3} \int v_\alpha(\boldsymbol{k}) f(\boldsymbol{r},\boldsymbol{k},t) d\boldsymbol{k}. \tag{103}$$

The electron current density equals zero at the equilibrium. It follows to replace $f(\boldsymbol{r},\boldsymbol{k},t)$

just by $\delta f(\boldsymbol{r}, \boldsymbol{k})$:

$$j_\alpha(\boldsymbol{r}) = -\frac{2e}{(2\pi)^3} \int v_\alpha(\boldsymbol{k}) \delta f(\boldsymbol{r}, \boldsymbol{k}) d\boldsymbol{k}. \tag{104}$$

Using the linear relation $\boldsymbol{j}^\alpha = \sigma_{\alpha\beta} \boldsymbol{E}_\beta$ under the zero temperature gradient condition and Eq. 102, the electrical conductivity tensor in the RTA $\sigma_{\alpha\beta}(\boldsymbol{r})$ is given by:

$$\sigma_{\alpha\beta}(\boldsymbol{r}) = \frac{2e}{(2\pi)^3} \int \tau(\boldsymbol{k}) v_\alpha(\boldsymbol{k}) v_\beta(\boldsymbol{k}) \left(-\frac{\partial f_0(\boldsymbol{k}, \boldsymbol{r})}{\partial \epsilon} \right) d\boldsymbol{k}. \tag{105}$$

The first law of thermodynamics applied to small region around $\boldsymbol{r}$ define heat density q:

$$dq \equiv T\, ds = d\epsilon - \mu\, dn, \tag{106}$$

where s, ϵ, and n are the entropy, energy, and number density. The heat density $\boldsymbol{j}_q$ is then defined as:

$$\boldsymbol{j}_q \equiv \boldsymbol{j}_\epsilon + \mu(\boldsymbol{r}) \boldsymbol{j}_n \tag{107}$$

The energy current density $\boldsymbol{j}_\epsilon$ is determined from:

$$\boldsymbol{j}_e \equiv \frac{2}{(2\pi)^3} \int \epsilon(\boldsymbol{k})\, \boldsymbol{v}(\boldsymbol{k})\, \delta f(\boldsymbol{r}, \boldsymbol{k}) d\boldsymbol{k} \tag{108}$$

and the number density $\boldsymbol{j}_n$ can be expressed by the electrical current density $\boldsymbol{j}$

$$\boldsymbol{j} \equiv -e \boldsymbol{j}_n. \tag{109}$$

Substituting Eq. 108 and 109 into Eq. 107, we get the heat density $\boldsymbol{q}$:

$$\boldsymbol{j_q} = \frac{2}{(2\pi)^3} \int [\epsilon(\boldsymbol{k}) - \mu(\boldsymbol{r})] \boldsymbol{v}(\boldsymbol{k}) \delta f(\boldsymbol{r}, \boldsymbol{k}) d\boldsymbol{k}. \tag{110}$$

Finally, the electron thermal conductivity tensor $\kappa_{\alpha\beta}$ is obtain from $j_{\boldsymbol{q}} = \kappa \nabla T$ under the condition of zero electrical current:

$$\kappa^{ij} = \frac{1}{4\pi^3 T(\boldsymbol{r})} \int [\epsilon(\boldsymbol{k}) - \mu(\boldsymbol{r})]^2 \boldsymbol{v}^\alpha(\boldsymbol{k}) \boldsymbol{v}^\beta(\boldsymbol{k}) \tau(\boldsymbol{k}) - \left(\frac{\partial f_0(\boldsymbol{r}, \boldsymbol{k})}{\partial \epsilon} \right) d\boldsymbol{k}. \tag{111}$$

2.9 Actinides

The actinide elements are 15 chemical elements with atomic numbers 89 through 103. Actinide series starts with actinium and ends with lawrencium. The core and semi-core electrons are $1s^2\ 2s^2\ 2p^6\ 3s^2\ 3p^6\ 3d^{10}\ 4s^2\ 4p^6\ 4d^{10}\ 5s^2\ 5p^6\ 4f^{14}\ 5d^{10}\ 6s^2\ 6p^6$ shells. The valence electrons occupy $5f$, $6p$ and $7s$ orbitals [30].

Heavy atomic nuclei and the presence of $5f$ electrons result in a great variety of unique properties:

- All actinides beyond uranium are non-naturally occurring due to short half-lives and were artificially prepared.
- All actinide isotopes are radioactive.
- They have very large atom radii in all forms.
- Their metals exhibit an unusual range of physical properties due to $5f$ electrons, *e.i.* plutonium has six allotropes [31].

2.9.1 5*f*-electrons and their dual nature

Electrons in solid-state can be localized or itinerant. Electrons with a small angular quantum number (s and p states) delocalize easily, whereas electrons with a high angular quantum number (particularly f states) remain their atomic character until higher densities [32].

Electrons want to be delocalized due to the minimization of kinetic energy. But if the on-site repulsive Coulomb energy (the cost of putting two electrons on the same lattice site) gets higher than the saving of kinetic energy, it prevents them from hopping and they stay localized [16, 32].

The $4f$ electrons are the first f electrons and therefore their wavefunction has a very short radius from the nucleus. Mostly, $4f$ electrons are shielded by $5s^2$ and $5p^6$ orbitals and they are not able to establish chemical bonds. They stay localized and, together with the strong spin-orbit coupling, have the perfect property for permanent magnets [32, 33]. The radial wavefunction of $5f$ electrons extends much farther from the nucleus which opens up the possibility of establishing a chemical bond [34]. However, the $5f$ electrons see their centrifugal potential caused by their high angular momentum ($\mathrm{l} = 3$) and they have to tunnel the potential barrier to become itinerant. As a result, the part of $5f$ electrons forms a chemical bond and the part remains localized. This makes them unique among all other materials [30].

The correct description of 5f electrons is required because material properties strongly depend on the ratio between itinerant or localized nature [32]. Moreover, this ratio depends on conditions such as temperature and applied pressure and it makes actinide physics complex [31].

2.9.2 Thorium

Thorium (Th), the second actinide element, is a weakly radioactive silvery metal with atomic number 90. From the thorium position in the periodic table, one could assume that *fcc* thorium should possess the hexagonal close-packed (hcp) crystal structure as other elements in group IVA elements (Ti, Zr, and Hf). However, among these tetravalent elements, thorium is the only one that holds the *fcc* crystal structure. It is believed to be attributed to the presence of the $5f$ states involved in chemical bonds [35]. Without occupation of the $5f$ states, thorium would hold the body-centered cubic (bcc) crystal structure and would exhibit normal tetravalent d metal behavior as in the case of Ti, Zr, and Hf [35]. Only when the $5f$ state occupation is taken into account, the *fcc* structure becomes the ground-state structure in agreement with experiments.

Typical applications of thorium compounds include incandescent gas mantles, production of ceramics, carbon arc lamps, coatings for tungsten welding rods, refractive glass additives, and heat-resistant laboratory crucibles. Thorium can also be used as a catalyst [31]. However, current attention paid to this element is due to possible use as a nuclear fuel in the generation IV nuclear reactor [36]. Thorium is 3 to 4 times more abundant than uranium while widely distributed in nature as an easily exploitable resource in many countries. Unlike uranium where it is necessary to distinguish the 'fissile' ^{235}U isotope and ^{233}U isotope, thorium can be found only in 'fertile' ^{232}Th isotope. Moreover, the thorium fuel cycle produces less radiotoxic waste than the uranium fuel cycle [37].

2.9.3 Thorium carbides

Carbide is a chemical compound of carbon with less electronegative elements. Actinides form three types of stoichiometric carbides – monocarbides (AnC), dicarbides (AnC_2), and sesquicarbides (An_2C_3).

The occurrence of monocarbide and dicarbide is reported for protactinium, thorium, uranium, neptunium, and plutonium. Sesquicarbides are found for thorium, uranium, neptunium, plutonium, americium, and curium [38].

The chemical bonding of actinide carbide is complex. The ionic, covalent, and metal bonding is present. The ionic bonding comes from the electronegativity difference between actinide and non-actinide element and the covalent bonding is present due to strong hybridization of actinide $6d$ and carbon $2p$ states [38].

The beginning of the research on actinide carbides as a nuclear fuel dates back to the 1950s. Then the research was stopped due to the ban on fast reactors for civilian purposes. It changed the focus on currently used fuels as uranium dioxide and mixed uranium-plutonium oxides.

The actinide carbide research has been restored in the last years and actinide carbides are the possible nuclear fuel of generation IV nuclear power plants [36]. Actinide carbides posse a lot of advantages over currently used oxides. They have higher burn-up, density, temperature operation, thermal conductivity, and better compatibility with clad materials [38, 39].

This work deals with thorium monocarbide which can be used as a fertile material in breeder reactors. The natural occurring ^{232}Th isotope absorbs a thermal neutron to produce an intermediate product ^{232}Pa with 27 days half-time by the β^- decay [37]. Then, the second β^- decay happens and fissile ^{233}U is obtained.

3 Methodology

Both thorium metal (Th) and thorium monocarbide (ThC) crystallize in $Fm\bar{3}m$ space group (No. 225) at ambient conditions. It means the face-centered cubic (*fcc*) structure for thorium and the rocksalt structure for thorium monocarbide. The rocksalt structure consists of two *fcc* structures shifted by half lattice parameter. Both structures are shown in Fig. 6. As far as magnetism is concerned, both are paramagnetic [40, 41].

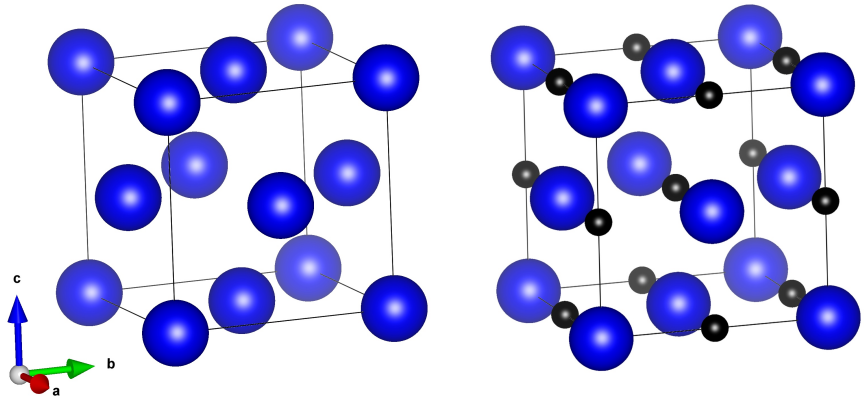

Figure 6: The the *fcc* structure of Th and the rocksalt structure of ThC.

The DFT calculations are carried out using the Vienna Ab Initio Simulation Package (VASP) [42] with the projector augmented wave scheme (PAW) [43, 44]. The exchange and correlation potentials are treated within the generalized gradient approximation of Perdew-Burke-Ernzerhof (GGA-PBE) [45] as well as with its revised version, the so-called PBEsol [46]. Valence electrons for thorium are in the $6s^2\,6p^6\,6d^1\,7s^2\,5f^1$ shells and the $2s^2\,2p^2$ configuration for carbon.

The kinetic energy cut-off for the plane-wave basis functions is set to 500 eV. Brillouin zone integrations are done out using a 16x16x16 Γ-centered k-point mesh for *fcc* thorium and a 12x12x12 Γ-centered k-point mesh for thorium monocarbide. The Hubbard model in the rotationally invariant approach [20] with $J = 0.4$ eV calculated from empirical rule $J = 0.33 + 0.070(Z - 89)$ [47] is used to correlate thorium $5f$ states.

The 4x4x4 supercells containing 64 atoms with the 6x6x6 Γ-centered k-point mesh for *fcc* thorium and the 2x2x2 supercells containing 64 atoms with the 4x4x4 Γ-centered k-point mesh for rocksalt structure of thorium monocarbide is used to calculate vibrational properties using the direct force-constant method as implemented in the PHONOPY [23] code and concurrently used to calculate the phonon thermal conductivity by solving the Boltzmann transport equation within the RTA for phonons iteratively through third-order interatomic force constants based on the small displacement method using the PHONO3PY [28].

The electrical and thermal conductivity is determined by the semi-classical Boltzmann theory as implemented in the BoltzTraP2 code [48] from 50 000 irreducible k-points in the unit cell.

The convergence criteria for the total energy and residual Hellmann-Feynman forces are set to 10^{-7} eV and 10^{-6} eV/Å, respectively. Bulk moduli were obtained from fits to Vinet's equation of state [49]. The components of the elastic tensor are obtained from the strain-stress relationship [50].

4 Results and Discussion

4.1 Electronic structure of *fcc* thorium

Precise determination of the electronic structure is crucial for the accurate and realistic description of lattice dynamics. Therefore, a thorough analysis of the SOC effect on the electronic structure is done.

First, a modification of the electronic structure upon the SOC applied to only the $6d$ and $5f$ states is presented in Fig. 7. It is difficult to find a difference between the solution with and without the SOC on $6d$ and $5f$ electrons. A slight change in the lattice parameter from 5.0523 Å to 5.0522 Å confirms that the $6d$ and $5f$ states are not affected by the SOC in this system.

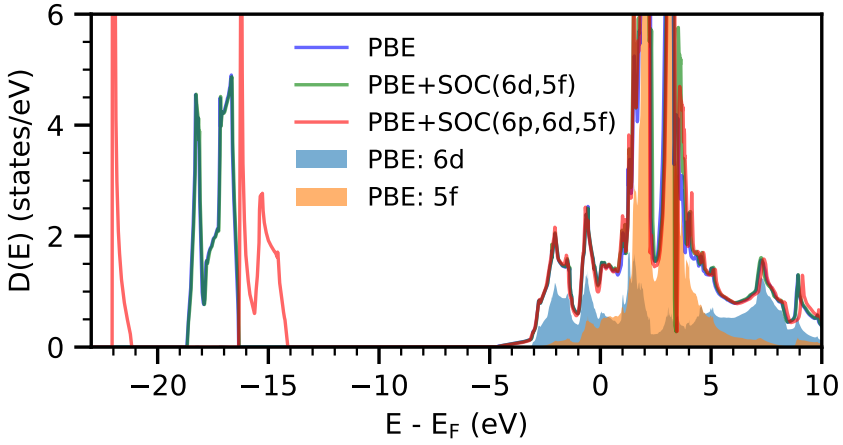

Figure 7: The total densities of electron states $D(E)$ for *fcc* Th with the SOC neglected and included. The filled lines represent the $6d$ (blue) and $5f$ (orange) states of the PBE model [6].

If the SOC is applied to all electrons, including the $6p$, the vicinity of the Fermi energy composed of the $6d$ and $5f$ states does not seem to be changed as well. The $6p$ states located around -18 eV are split into well-separated $6p_{1/2}$ and $6p_{3/2}$ states by about 6 eV. However, the $6p_{1/2}$ states are not described correctly because scalar relativistic p states are zero at the origin, but fully relativistic Dirac $6p_{1/2}$ states are not. So it is impossible to represent these $p_{1/2}$ states with a linear combination of scalar relativistic basis functions. This problem occurs if the second variational approach is used. In the second variational approach, the scalar relativistic Hamiltonian is diagonalized first, and then given scalar eigenvectors and eigenvalues are used as a limited basis set for diagonalizing the full Hamiltonian with the spin-orbit coupling [51, 52, 53].

Mattsson and Wills [53] compare the second variational approach with the Dirac solution. They observe the shift of the $6p_{1/2}$ states to lower energy and as a result, the increase of $6p_{1/2}$-$6p_{3/2}$ splitting by additional 1.3 eV. This result is consistent with the Kuneš *et al.* approach [52], where additional local orbitals are added to mimic the correct behavior of relativistic p-states within full potential linearized augmented plane wave methodology (FLAPW).

Nevertheless, these two approaches are not consistent concerning the equilibrium volumes. Both predict the equilibrium volume reduction for the second variational approach but differ in assuming the equilibrium volume with the $6p_{1/2}$ state corrected base. Mattsson and Wills [53] report an increase in the volume of 0.3 %, but Kuneš *et al.* [52] report a reduction of around 1 %. The Dirac solution should be more precise in principle, but they use the atomic-sphere approximation, which is less accurate method than the FLAPW. The second variational approach, which is used in this work, reduces the equilibrium volume around 1.6 %.

A comparison of the Sommerfeld coefficients (listed in Table 2) between PBE, PBE+SOC (6*d*,5*f*), and PBE+SOC(6*p*,6*d*,5*f*) confirms that the electronic density does not change significantly near the Fermi energy (E_F). However, the PBE+SOC(6*p*,6*d*,5*f*) model gives a better result when compared to the experimental measurements [54, 55] than the model without SOC.

This is based on 10 % less DOS at the Fermi energy and the smaller electron-phonon coupling parameter ($\lambda = 0.456$) [56] using the SOC scheme in comparison with the scalar-relativistic scheme ($\lambda = 0.577$) [56]. The difference between PBE and PBE+SOC(6*d*,5*f*) comes only from the different the electron-phonon coupling parameter

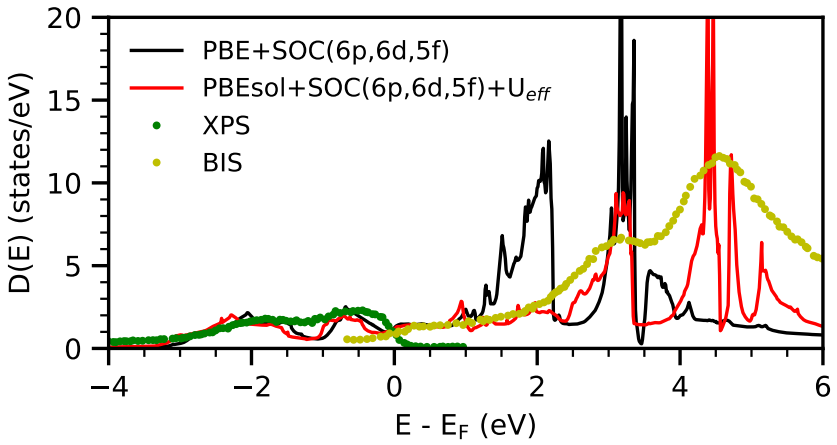

Figure 8: The total electron density of states $D(E)$ of *fcc* Th for two different exchange and correlation potentials presented together with the BIS and XPS measurements [6, 7].

The density of states accuracy can be checked with Bremsstrahlung Isochromat Spectroscopy (BIS) and X-ray Photoelectron Spectroscopy (XPS) measurements. Figure 8 shows that our result of PBE+SOC(6*p*,6*d*,5*f*) agrees with the XPS experiment but fails with the BIS experiment. The PBEsol exchange and correlation potential is also utilized to see if it can reproduce the BIS experiment. The lattice parameter of PBEsol+SOC(6*p*,6*d*,5*f*) yields 4.933 Å and is considerably lower than the experimental 5.085 Å [57]. The Hubbard model to 5*f* electrons is applied to increase the localization of the 5*f* states. The large Hubbard U ($U = 4eV$) is needed to get the lattice parameter of 5.069 Å, which is close to experimental values. Figure 8 shows that this model reproduce both the XPS and the BIS experiment [7].

The high value of the Hubbard U parameter acting on the 5*f* states is needed for the correct

Table 2: The calculated and experimental lattice parameters (a), elastic constants c_{ij}, bulk modulus B, Sommerfeld coefficient γ, and Debye temperatures θ_D of *fcc* Th

Th	E_{xc}	U_{eff} (eV)	a (Å)	c_{11} (GPa)	c_{12} (GPa)	c_{44} (GPa)	B (GPa)	γ (mJ/K^2/mol)	θ_D (K)	Rerefence
VASP	PBE	0.0	5.052	76.3	43.4	51.3	53.2	5.12	182	This work
	PBE+SOC(6*d*,5*f*)	0.0	5.052	76.0	43.4	50.9	53.5	4.73	181	This work
	PBE+SOC(6*p*,6*d*,5*f*)	0.0	5.024	81.8	45.4	54.6	57.7	4.27	181	This work
	PBEsol+SOC(6*p*,6*d*,5*f*)	4.0	5.069	75.9	59.8	40.1	63.8	4.02	151	This work
FP-LMTO			4.910	55	35	46	63			Söderlind[58, 59]
ABINIT	PBE	0.0	5.024	84	40	58	55			Bouchet[60]
WIEN2K	PBE	0.0	5.062	76	41	53	57			Gupta[61]
Model pot.				78	62	40	68			Baria[62]
VASP	PBE	0.0	5.062	81	41	49	50			Hu[63]
WIEN2K	PBE	0.0	5.080	76	44	44	55			Jaroszewicz[64]
Exp.			5.085	81	50	50	60			Greiner[57]
Exp.			5.089	78	48	51	58			Armstrong[65]
Exp.								4.23	167	Schmidt[54]
Exp.								4.31	163	Gordon[55]

description of states high above the Fermi energy (E_F) of thorium, which is consistent with localized behavior of the $5f$ states in heavier actinides.

Regardless, such strong localization of the $5f$ states in *fcc* thorium has no physical meaning because only 0.3 electron is occupied in $5f$ shells. Such a small number cannot be correlated. This type of the exchange and correlation potential should be used only for calculation of optical properties due to a good description of unoccupied states.

4.2 Elastic properties of *fcc* thorium

Concerning mechanical properties of *fcc* thorium, several theoretical works have been conducted [58-64] with different methods and treatment of electron exchange and correlation effects, but none of them can reproduce all elastic constants. Only a few authors [58, 59] take into account the spin-orbit coupling.

The results of this work are presented in Table 2 and compared to the ones obtained with other theoretical and experimental studies. All previous theoretical calculations [58-64] fail to fully reproduce all elastic constants at the same time, mainly c_{12}, which is in most calculations significantly underestimated.

This work have the same problem. The c_{12} is greatly underestimated without SOC. The inclusion of SOC only to $6d$ and $5f$ electrons has a weak effect on elastic constants. When SOC is also included to $6p$, the problematic c_{12} increases but simultaneously it also increases c_{44} further away from experimental values. The elastic constant c_{11} get overestimated, but closer to the experiment [57, 65] than without the SOC.

In summary, the inclusion of the SOC for the $6p$ states has a significant impact on the elastic constants of *fcc* thorium. The inaccurate description of the $6p_{1/2}$ can be the decisive reason

why the theoretical works are not able to fully reproduce all elastic constants concurrently. The supporting argument is based on an increase of the bulk modulus from 54.5 GPa to 58.3 GPa when the fully-relativistic scheme is used [53]. The reported value is very close to the experimental values 58 and 60 GPa [57, 65].

The elastic constants of PBE+SOC(6*d*,5*f*) support the previous statement that the SOC for 6*d* and 5*f* states has only a minor effect on the system and can be neglected.

Although only the PBEsol exchange and correlation potential gives excellent agreement with the XPS and BIS measurements, it fails to reproduce the experimental elastic coefficients and bulk modulus. A such a strong localization is not physical for *fcc* thorium and is an artificial correction. For this reason, this model is not investigated further.

4.3 Lattice dynamics of *fcc* thorium

There is only one unique atom in its primitive cell for *fcc* thorium. Thus there are only three independent phonon modes in dispersion relations. The phonon dispersion curves of *fcc* thorium as calculated along several symmetry directions for the PBE exchange-correlation potential are presented in Fig. 9.

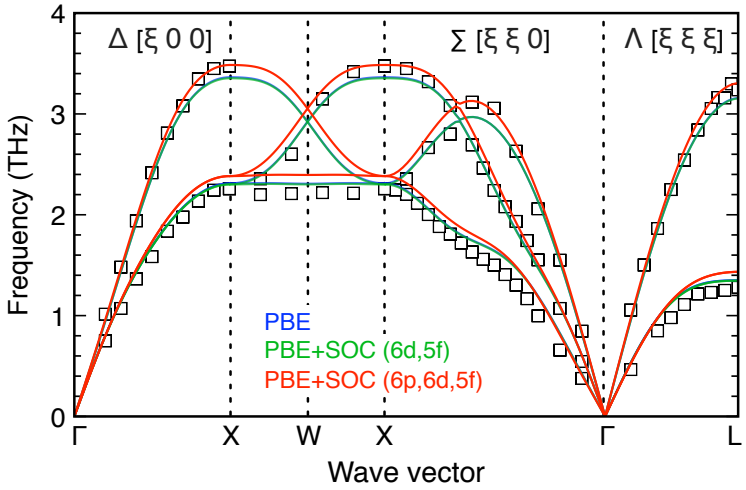

Figure 9: The dispersion relations of *fcc* Th phonons [6]. The blue line represents PBE, the green line represents PBE+SOC(6*d*,5*f*), the red line represents PBE+SOC(6*p*,6*d*,5*f*), and the black squares are the experimental data [8].

The directions $\Delta[\xi\ 0\ 0]$, $\sum[\xi\ \xi\ 0]$, and $\Lambda[\xi\ \xi\ \xi]$ are carried out at zero temperature with the comparison of the experimental data obtained from the neutron-scattering measurement at ambient conditions [8]. Figure 9 reveals that the shift to higher frequencies from the inclusion of the SOC(6*p*,6*d*,5*f*) is needed to describe dispersion relations of the longitudinal phonon branches correctly. However, it overestimates the frequency of the transverse phonon branches at the same time. It means that the shift comes from the volume change. The same shift is reported in

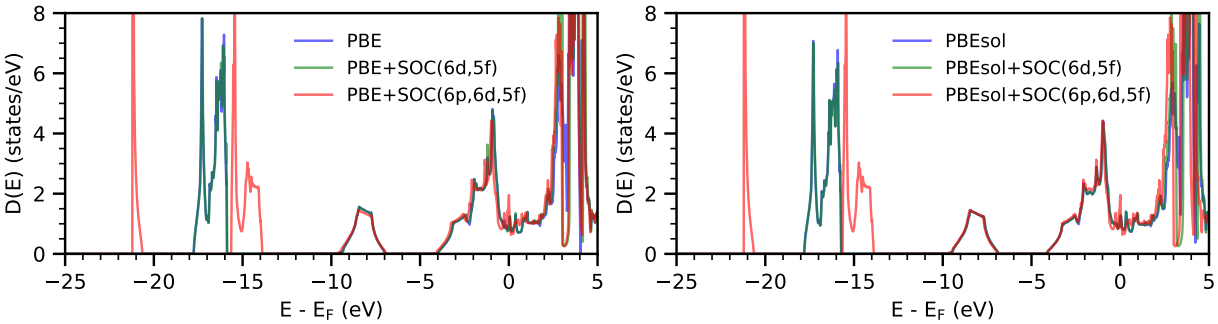

(a) the PBE potential (b) the PBEsol potential

Figure 10: The total densities of electron states $D(E)$ for ThC [6].

previous theoretical work [56]. In accord with our previous findings, the SOC(6*d*,5*f*) has minimal impact on the phonon spectrum.

All models reproduce the anomalous behavior of the transverse branches along the $\sum[\xi\ \xi\ 0]$ direction even though the electron-phonon interaction is not included. It follows that this anomaly does not arise from the electron-phonon interaction as claimed by experimentalists [8].

It is concluded that the spin-orbit coupling acting on $6d$ and $5f$ is only a small perturbation. On the contrary, the spin-orbit coupling acting on $6p$ semi-core electrons can be too big perturbation to handle it by the second-variational approach.

4.4 Electronic structure of thorium monocarbide

Figure 10a shows a modification of the electronic structure of ThC upon the SOC. The same trend as for *fcc* thorium is observed: the inclusion of the SOC to the $6d$ and $5f$ electrons has almost zero effect on the DOS. However, a moderate modification of the DOS around the vicinity of the Fermi energy within the inclusion of the SOC to the $6p$ states (indirect effect of the semi-core $6p$ states) is found. The peaks of the DOS get sharper than in the scalar-relativistic solution without the SOC.

The PBEsol exchange-correlation potential has been proved to be successful for uranium monocarbide [66]. It is reasonable to investigate this potential for ThC as well. Figure 10b shows a modification of the electronic structure of ThC upon the SOC. There is no significant difference between both exchange-correlation potentials from the electron structure point of view, *i. e.* almost zero difference with the SOC(6*d*,5*f*) inclusion and the sharper shape around the Fermi energy with the SOC(6*p*,6*d*,5*f*). The emerging peaks around E_F come from the hybridization of the Th $6d$, Th $5f$, and C $2p$ states, as shown in Fig. 11.

Surprisingly, the SOC(6*p*,6*d*,5*f*) does not seem to improve the DOS, but quite the contrary. The Sommerfeld coefficients of both exchange-correlations potentionals (PBE/PBEsol) indicate that the more accurate DOS is based on the model without the SOC on the $6p$ states because its values of 2.07/2.76 $mJK^{-2}mol^{-1}$ are much closer to the experimental values (2.1–2.9 $mJK^{-2}mol^{-1}$) [67, 68] than 4.51/4.11 $mJK^{-2}mol^{-1}$ obtained with SOC. The high values of

the Sommerfeld coefficient come from the sharp peaks that appears by adding the SOC to the $6p$ states. Moreover, the calculated values do not include the electron-phonon many-body enhancement factor and therefore should be smaller than the experimental ones [67, 68].

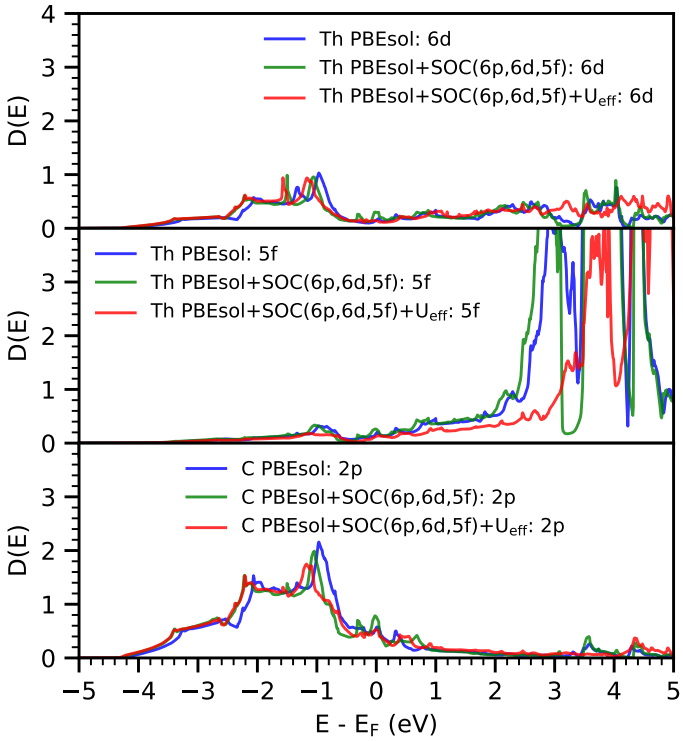

Figure 11: The projected densities of electron states $D(E)$ for ThC calculated with PBEsol, PBEsol+SOC($6p$,$6d$,$5f$), and PBEsol+SOC($6p$,$6d$,$5f$) with the Hubbard U_{eff} = 3 eV [6].

4.5 Elastic properties of thorium monocarbide

The bulk modulus (B) is the only elastic property that was measured for thorium monocarbide. However, experimental studies are not consistent. Gerward *et al.* [69] report B = 109 GPa while Yu *et al.* [70] B = 147 GPa. Olsen *et al.* [71] claim that the discrepancy is possibly due to the difference of stoichiometry. The sample of Yu *et al.* [70] had a composition corresponding to $ThC_{0.95}$ but Gerward *et al.* [69] have a much less stoichiometric $ThC_{0.76}$. The higher value is supported by comparison with the lattice parameters and the bulk moduli of thorium nitride (ThN) and thorium sulphide (ThS) [70].

Both PBE and PBEsol predict the bulk modulus to 136 GPa. This is about 7.5 % deviation from the experiment [70]. The inclusion of the SOC only on $6d$ and $5f$ has no effect for PBEsol and only a weak effect for PBE, as listed in Table 3. Decreasing the bulk modulus of PBE is based on decreasing c_{12} which, however, is partly offset by increasing c_{11}. All elastic constants slightly decrease for PBEsol. If the SOC also include $6p$ states, the PBE bulk modulus changes from 135 GPa to 127 GPa, in contrast with much a smaller change from 137.3 GPa to 135.6

Table 3: The calculated and experimental lattice parameters (a), elastic constants c_{ij}, bulk modulus B, Sommerfeld coefficient γ, and Debye temperatures θ_D of ThC

ThC	E_{xc}	U_{eff} (eV)	a (Å)	c_{11} (GPa)	c_{12} (GPa)	c_{44} (GPa)	B (GPa)	γ (mJ/K^2/mol)	θ_D (K)	Rerefence
VASP	PBE	0.0	5.354	222.9	93.6	80.1	135.2	2.07	314	This work
VASP	PBE+SOC(6*d*,5*f*)	0.0	5.354	225.3	89.4	79.7	134.9	2.06	295	This work
VASP	PBE+SOC(6*p*,6*d*,5*f*)	0.0	5.335	222.0	86.8	78.5	127.3	4.51	303	This work
VASP	PBEsol	0.0	5.301	240.0	90.2	78.4	137.3	2.76	335	This work
VASP	PBEsol+SOC(6*d*,5*f*)	0.0	5.301	239.4	90.1	78.0	137.3	2.82	334	This work
VASP	PBEsol+SOC(6*p*,6*d*,5*f*)	0.0	5.279	240.0	87.6	77.0	135.6	4.11	320	This work
VASP	PBEsol+SOC(6*p*,6*d*,5*f*)	3.0	5.328	264.1	83.2	83.5	144.7	2.46	342	This work
WIEN2k	PBE	0.0	5.388	252	96	60	148	1.71		Shein [72]
WIEN2k	PBE+SOC	0.0	5.388	163	70	54	100	2.59		Shein [72]
CASTEP	PBE	0.0	5.341	276	99	87	158		458	Aydin [73]
CASTEP	LDA	0.0	5.269	241	96	78	145		478	Aydin [73]
CASTEP	LDA+U	2.3	5.336	215	88	81	130		470	Aydin [73]
ESPRESSO	PBE	0.0	5.335	222	86	66	131		298	Daroca [74]
VASP	PBE	0.0	5.348	216	89	80	137		258	Sahoo [75]
Exp.			5.335							Street [76]
Exp.			5.322				109			Gerward [69]
Exp.			5.340				147			Yu [70]
Exp.								2.9	280	Harness [67]
Exp.			5.344					2.1	262	Danan [68]

GPa for the PBEsol. Nevertheless, it gives worse agreement with an experimental value of 147 GPa in both cases. Other theoretical works (see Table 3) are not uniform in this matter.

Decreasing of the bulk modulus/elastic constants with smaller volume is in direct contrast to *fcc* thorium, where the opposite effect is reported. It shows that chemical bonding of ThC is much more complex due to the carbon presence.

4.6 Phonon DOS of thorium monocarbide

Actinide monocarbides are systems with two elements with significantly different atomic masses. Carbon is approximately 20 times lighter than an actinide element. As a result, a phonon spectrum is divided into low-frequency phonons (acoustic branches) arising from oscillations of heavy actinide atoms, and high-frequency phonons (optical branches) arising from oscillations of light carbon atoms. A frequency gap separates these bands.

Figures 12a and 12b present the phonon densities of states for the PBE and PBEsol potentials. While both approaches describe well the acoustic phonon modes, the comparison with experiment measured by the time-of-flight technique [9] shows that both greatly underestimate the optical phonon modes. Similarly, an underestimated carbon phonon spectrum of PBE is reported by Daroca *et al.* [74] and Sahoo et al. [75].

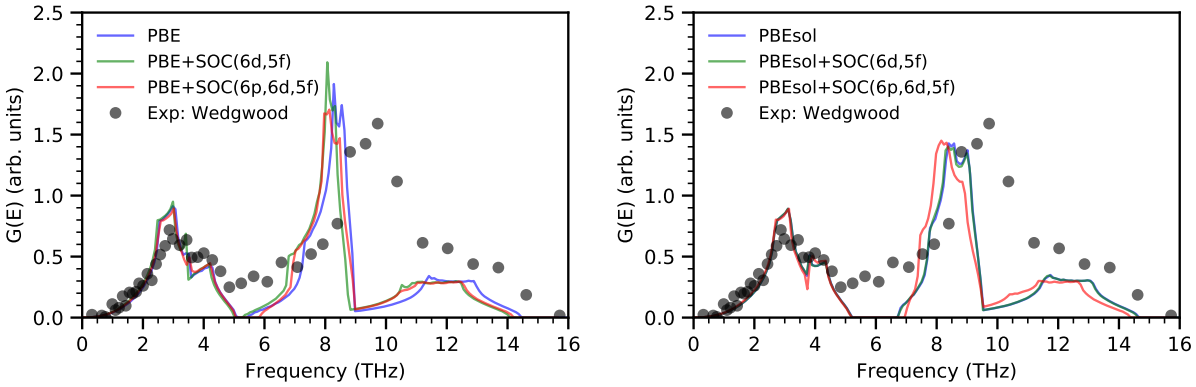

(a) The PBE potential

(b) The PBEsol potential

Figure 12: The phonon densities of states G(E) for ThC [6]. The TOF data (circles) are taken from Wedgwood [9].

The poor agreement with the experiment suggests that thorium and carbide bonding is much stronger than the models predict. It is consistent with the more than 7 % bulk modulus mismatch.

4.7 Thorium monocarbide with the Hubbard model

The same failure of the PBE potential to reproduce the optical branches is also well known for uranium monocarbide [66]. The authors solved this inconsistency with an experiment by including the SOC(6*p*,6*d*,5*f*) and the Hubbard model.

It is common practice to use the Hubbard model for uranium because uranium consists of $5f^3$ electrons which are partly correlated. However, it is unusual to use the Hubbard model for thorium, because of weak occupancy of the $5f$ states (around 0.3 electron).

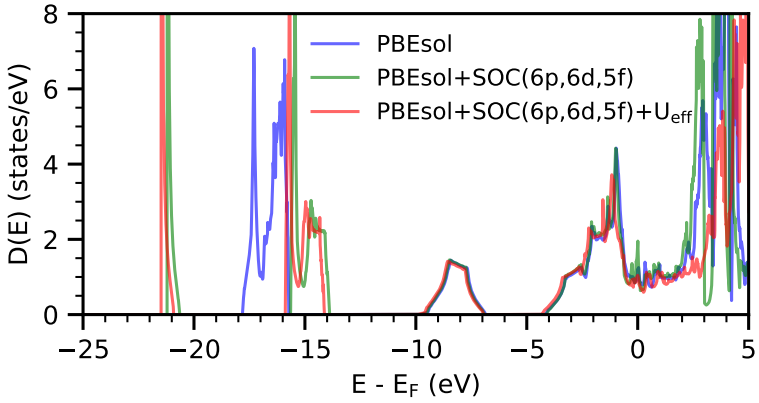

Figure 13: The total densities of electron states D(E) for ThC calculated with PBEsol, PBEsol+SOC(6*p*,6*d*,5*f*), and PBEsol+SOC(6*p*,6*d*,5*f*) with Hubbard $U_{\text{eff}} = 3$ eV [6].

The Hubbard model is only applied to PBEsol because PBEsol underestimates the lattice parameter. The PBE already overestimates the lattice parameter and the correct value of the volume is crucial for lattice dynamics.

Unlike for uranium in UC where the Hubbard model separates the $5f_{1/2}$ and $5f_{3/2}$ states, including the Hubbard model to thorium in ThC only shifts the $5f$ states to higher energies, as shown in Fig. 11. Thus, the occupation of the $6d$ states, which hybridizes better with the $2p$ states and increases the strength of the chemical bond, is raised. Table 3 shows that the bulk modulus increases to 145 GPa if the Hubbard model with $U_{eff} = 3$ eV is applied. The choice of $U_{eff} = 3$ eV is based on fitting the experimental lattice parameter. The predicted bulk modulus of 145 GPa is very close to the experimental 147 GPa [70].

While the $5f$ states are shifted to higher energies, all other states are shifted to lower energy, as shown in Fig. 11. It is good correction for the $6p_{1/2}$ states which should be in the lower energies as discussed above, but the 6 $p_{3/2}$ states are incorrectly also moved into lower energies, as shown in Fig. 13. It demonstrates that this treatment is artificial.

However, a better agreement with the experiment for the Sommerfeld coefficient is obtained because the sharp peaks at the vicinity of the Fermi energy get flattened. The value 2.46 $mJK^{-2}\,mol^{-1}$ is much closer to 2.1/2.9 $mJK^{-2}\,mol^{-1}$ [67, 68] than 4.11 $mJK^{-2}\,mol^{-1}$.

Furthermore, the great agreement with the experimental phonon density of states is found (see Fig. 14). Not only there is a perfect match at the optical frequencies, but also the acoustic ones are slightly better. Figure 14 shows phonon dispersion relations which are along the same directions as in *fcc* thorium. The biggest difference can be found in the direction $\Delta[\xi\ 0\ 0]$ whereas the phonon dispersion curves at the $\Lambda[\xi\ \xi\ \xi]$ direction are much less affected. It follows that greater occupation of the $6d$ states enhances directional chemical bonding.

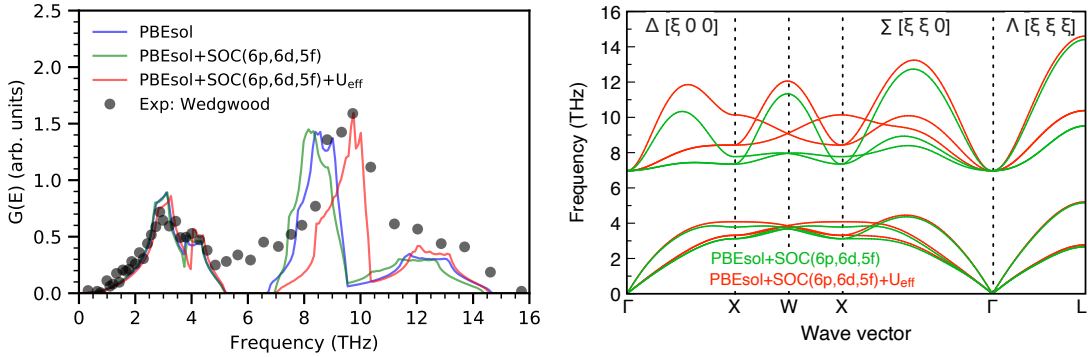

Figure 14: The phonon dispersion relations and the phonon densities of states G(E) for ThC [6]. The TOF data (circles) are taken from Wedgwood [9].

It can be concluded that the correct treatment of the spin-orbit coupling acting on the $6p$ states or special treatment of the $5f$ states is needed even for some thorium compounds and the simple DFT cannot be used in all cases.

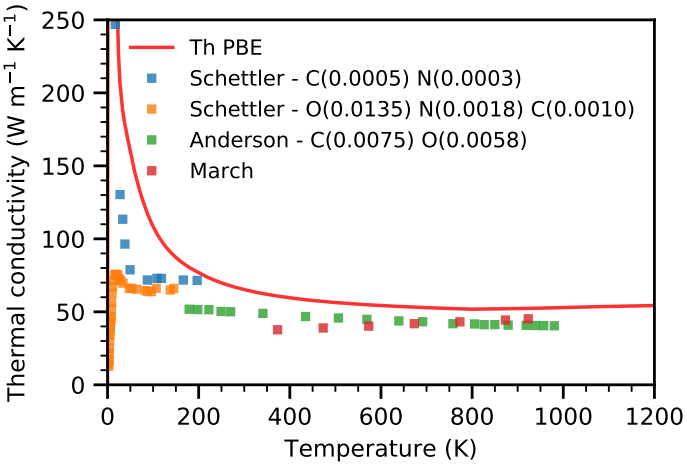

Figure 15: The total thermal conductivity of *fcc* Th [6]. The experimental values are from Schettler *et al.* [10] (blue and orange), Anderson *et al.* [11] (green), and March *et al.* [12] (red).

4.8 Thermal conductivity

Thermal conductivity is the most important property of nuclear fuel because it influences all processes such as swelling, grain growth, and fission gas release and limits linear power [77]. For the design of new nuclear materials, it is necessary to provide a method that can predict this material property under different conditions (stoichiometry, non-stoichiometry, *etc.*).

The thermal conductivity of metal is composed of two components, *i. e.* phonon and electronic part. The electronic part of thermal conductivity causes that metals have mostly several times higher thermal conductivity at high temperatures than isolators, which are commonly used as nuclear fuels nowadays.

4.8.1 Thermal conductivity of *fcc* thorium

The PBE exchange and correlation potential without the SOC is used for thermal conductivity analysis because the importance of the SOC on lattice dynamics is not demonstrated. First, the total thermal conductivity of *fcc* Th is determined by including only phonon-phonon interactions and compared with the experimental data [10-12]. Figure 15 shows that the theoretic prediction is in good agreement with the experiments at higher temperatures, which are more relevant to the actual operating conditions of nuclear reactors.

Understandably, the theory overestimates the experimental results in the low-temperature region because the model crystal is treated as fully stoichiometric without any defects or impurities. It is needed to include all contributions which affect phonon lifetimes:

$$\frac{1}{\tau} = \frac{1}{\tau_{pd}} + \frac{1}{\tau_{ld}} + \frac{1}{\tau_{vd}} + \frac{1}{\tau_{gb}} + \frac{1}{\tau_{is}} + \frac{1}{\tau_{e-ph}} + \frac{1}{\tau_{ph-ph}} \tag{112}$$

to simulate real crystals. The phonon lifetimes τ_{pd}, τ_{ld}, τ_{vd}, τ_{gb}, τ_{is}, τ_{e-ph}, and τ_{ph-ph} correspond to the phonon scattering by point defects (substitutional atoms, interstitials, and vacancies), line defects, volume defects, grain boundaries, isotope scattering, electron-phonon, and phonon-phonon interaction.

Assuming that a sample is well prepared, volume defects can be neglected. Isotope scattering is weak for these materials because thorium and carbide occur predominantly in only one isotope. Thermal conductivity at low temperatures is mostly affected by point defects and grain boundaries as mentioned in Section 2.8.2.

Schettler *et al.* [10] measured two sides of the same sample but with different impurity ratios. One side had composition of $Th_{0.9992}$ $C_{0.0005}$ $N_{0.0003}$ and the second one $Th_{0.9847}$ $C_{0.0135}$ $N_{0.0018}$. As shown in Fig. 15, the measured thermal conductivity of the more stoichiometric sample is up to 7 times higher at maximum than the less stoichiometric one.

However, the thermal conductivity is composed of two parts, *i. e.* electron and phonon one. It is needed to take into account the modification of lifetimes for electrons in the same matter to simulate real crystals.

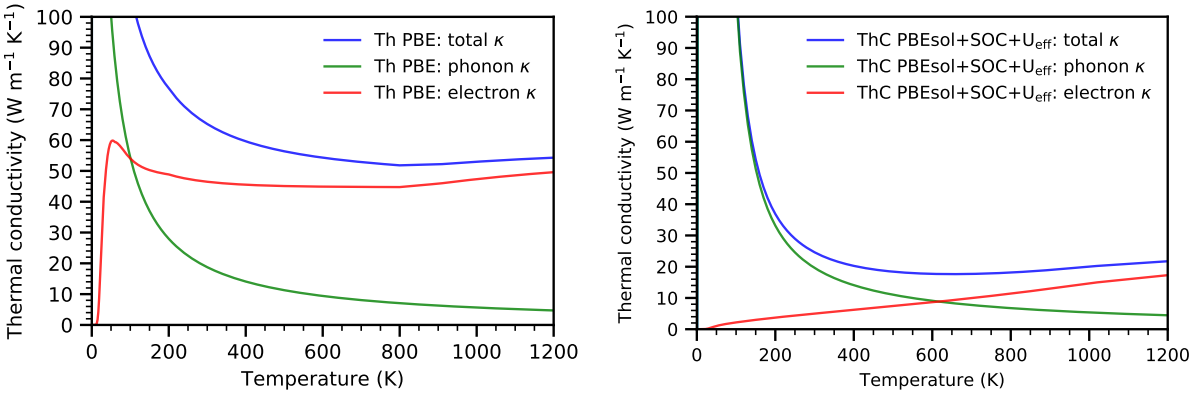

(a) *fcc* Th (PBE) (b) ThC (PBEsol+SOC+U_{eff} = 3 eV)

Figure 16: The phonon and electron parts of the thermal conductivity [6].

Figure 16a presents the total thermal conductivity of *fcc* thorium and its phonon and electron contributions. The maximum of the phonon thermal conductivity is found around 20 K. Then it decreases exponentially as the Umklapp processes become more important. It happens because the Umklapp processes require wavevectors $\boldsymbol{q}$ close to the border of the Brillouin zone. But these wavevectors have mostly high frequencies and their population is minor at low temperatures according to the Bose-Einstein statistics. As temperature increases, so does the probability of Umklapp processes, and the thermal conductivity decreases considerably.

The course of the electronic thermal conductivity is different from the phonon thermal conductivity. It rises sharply as electrons begin to acquire energy required for excitation into the conduction bands while the lattice vibrates with a small magnitude. As the temperature increases, the vibration amplitude increases and electron-phonon interactions intensifies. It results

that the relaxation times of electrons take high values at low temperatures ($10^{-13}s$) and sharply declines once the phonon-electron interactions intensify ($10^{-15}s$). The relaxation times of electron are determined using the experimental resistivity measurements [78, 79] in this work. After the peak of the electronic thermal conductivity around 40 K, there is a slight decrease and then almost a constant value. The balance between new conductive electrons and lower lifetimes is established.

In general, the thermal conductivity of *fcc* thorium is controlled primarily by the phonon part up to 60 K, where both parts are equal. Then the electronic contribution begins to dominate over the phonon one. At higher temperatures, one can even neglect phonons.

4.8.2 Thermal conductivity of thorium monocarbide

The only PBEsol+SOC(6*p*,6*d*,5*f*)+U(3 eV) model can reproduce the experimental phonon DOS. It is reasonable to use this model to obtain the thermal conductivity. There is a considerable difference in the thermal conductivity between *fcc* thorium and thorium monocarbide. This is apparent from the comparison of Figs. 16a and 16b. The total thermal conductivity of thorium monocarbide is more than twice as small as *fcc* thorium. The difference is based on the lesser electron part (the relaxation times of conductive electrons are derived from experimental resistivity measurements [80, 81]). It is consistent with the twice smaller value of the Sommerfeld coefficient and generally much weaker metallic behavior of thorium monocarbide. Concerning the phonon part, the phonon thermal conductivity of thorium monocarbide is slightly larger than in *fcc* thorium.

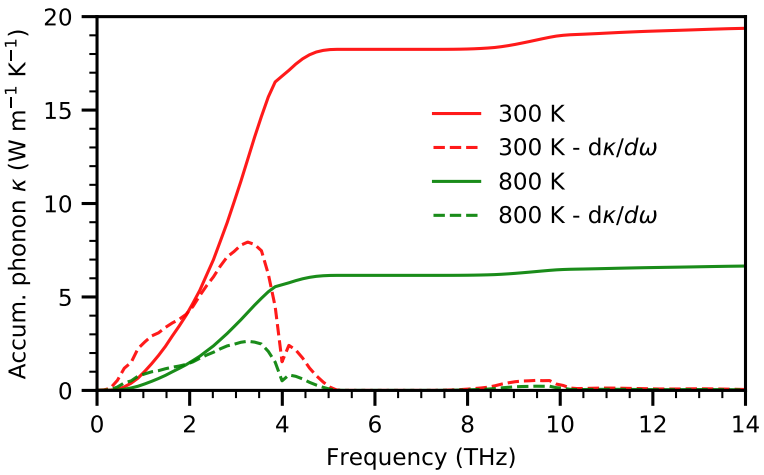

Figure 17: The accumulated phonon thermal conductivity as a function of the phonon frequency for ThC [6].

To analyze the phonon thermal conductivity of thorium monocarbide, the accumulated thermal conductivities at 300 K and 800 K and their derivatives with respect to the energy are plotted in Fig. 17. The acoustic branches contribute to 94 % of the phonon thermal conduc-

tivity. This result differs significantly from NpO_2 when the optical branches contribute to 27 % of the phonon thermal conductivity [82]. The optical branches of thorium monocarbide do not contribute significantly in the whole temperature range, as shown in Fig. 18.

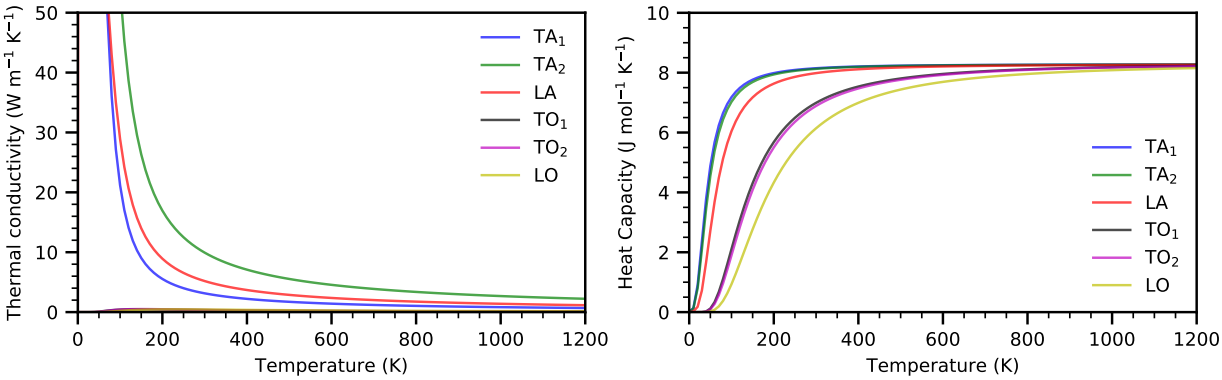

Figure 18: The phonon part and the heat capacity per mode of ThC as a function of T [6].

The phonon thermal conductivity is a function of the heat capacity, group velocity, and phonon lifetime of phonon mode according Eq. 84. Although there is a difference between the heat capacities for the acoustic and optical branches (see Fig. 18), it disappears at a higher temperature where the Bose-Einstein statistics go into classical the Maxwell-Boltzmann one. The difference is also found between the transverse and longitudinal branches where the former ones have higher heat capacity per mode at a lower temperature due to smaller vibrational frequencies. Nevertheless, the heat capacity does not seem to be a determining factor as the heat capacities of the optical modes are almost the same as the acoustic modes at 800 K; see Fig. 17.

The source of low optical contribution can also be the group velocity whose distribution is shown in Fig. 19. The optical modes have about twice the average group velocity of the acoustic ones. The most significant difference can be found at the longitudinal optical mode due to large dispersion (see Fig. 14).

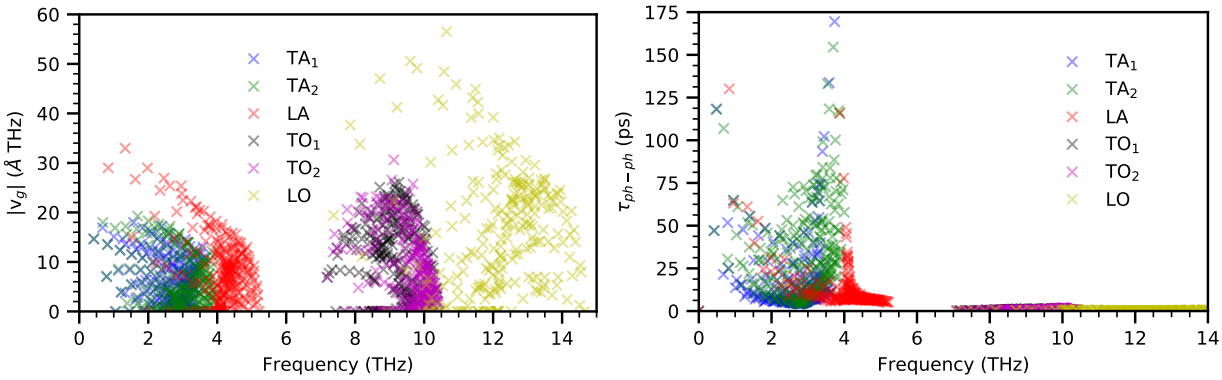

Figure 19: The group velocity in the xx direction and the phonon lifetime distribution of ThC as a function of the phonon frequency [6].

Although the group velocities of the optical branches are higher, the optical branches contribute to the total phonon conductivity only a little. It means that the group velocity is not a decisive factor. The final variable affecting phonon thermal conductivity is phonon lifetimes. Figure 19 explains why the optical phonon branches almost do not transfer heat. The phonon lifetimes of the optical modes are more than 25 times smaller than the lifetimes of the acoustic modes. The scattering of the optical phonon is vast, and therefore, these modes cannot effectively transfer energy (heat).

The same reason is also found for explanation of why the transverse acoustic mode (TA_2) has a greater contribution to the total phonon conductivity than the longitudinal acoustic mode (LA), as shown in Fig. 18. Though the average group velocity of the transverse mode is around 30 % smaller than the longitudinal one, the average phonon lifetime of the transverse acoustic mode (TA_2) is 3 times greater than the longitudinal acoustic mode (LA).

4.8.3 Grain boundary

The effect of grain boundary scattering can be easily simulated using:

$$\tau_{gb} = \frac{v_g}{L}, \tag{113}$$

where L is the boundary mean free path.

This model is based on the assumption that phonons are always scattered at the grain boundary. Although it is not a valid assumption, it can offer a qualitative insight into how the grain boundary affects the phonon thermal conductivity.

The phonon thermal conductivities of ThC with various grain sizes are presented in Fig. 20. It confirms enormous sensitivity at low temperatures and minor sensitivity at high temperatures, where Umklapp scattering prevails.

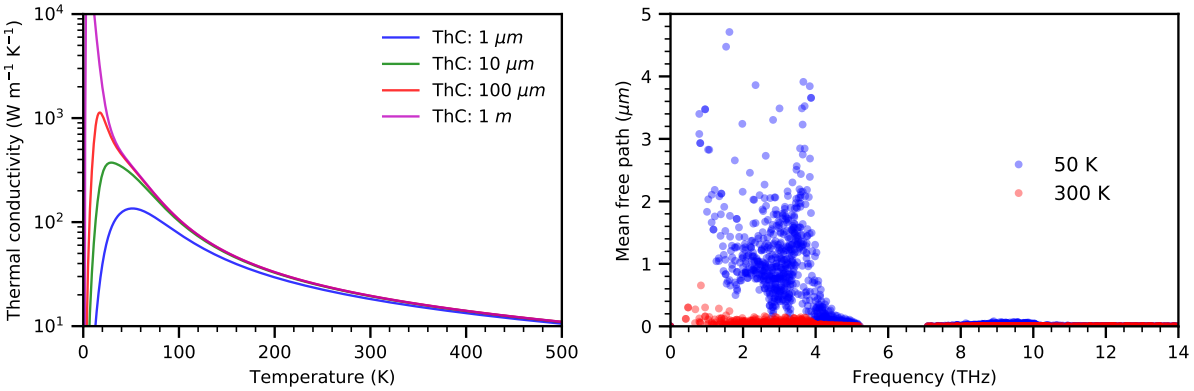

Figure 20: The phonon thermal conductivity with a various grain sizes and the phonon mean free path of ThC (PBEsol+SOC+U_{eff}).

Although the thermal conductivities of polycrystals with a grain size of 10 μm, 100 μm, and 1 m differ significantly at very low temperatures, only a slight difference is found from around

80 K. Different behavior is observed for polycrystal with 1 μm grain size where the thermal conductivity is slightly lower even at higher temperatures.

It can be explained by the mean free path as shown in Fig. 20. The mean free path of the phonon is a few micrometers at 50K. In a 1 m polycrystal, scattering at the boundaries have an insignificant effect. The phonon scatters on average 100 times before it hits the grain boundary in a 100 μm polycrystal. However, in a 10 μm polycrystal, approximately every tenth scattering takes place at the grain boundary. Finally, the scattering at the grain boundary is significant in 1 μm polycrystal as it occurs with the same probability as the phonon-phonon scattering. At higher temperatures, the average mean free path is around 0.05 μm. It follows that the scattering at the grain boundary has a minimal effect for polycrystals with a grain size of several μm. The normal grain size of nuclear fuels is around 10 μm [83]. It concludes that grain size is not a limiting factor of thermal conductivity for nuclear fuels due to operating at high temperatures.

4.8.4 Mass-difference defects

Phonons scatter on defects due to density fluctuations and variations in elastic constants. Assuming that density fluctuations outweigh the variation of elastic constants, a simple model including only the scattering on density fluctuations is given by [4]:

$$\tau_{pd} = \frac{2v_g^3 N}{\pi\omega^4} \sum_i \frac{\overline{M^2}}{x_i(M_i - \overline{M})^2} \tag{114}$$

where N is the number of unit cells per unit volume, x_i is the concentration of unit cells of mass M_i, and $\overline{M}$ is the average mass per unit cell.

Equation 114 provides some interesting findings. The probability of scattering on the mass-difference defect decreases with the cube of the group velocity and increases with the fourth power of the frequency. It is because faster phonon modes have a shorter time to interact with the defects than slower ones and higher frequencies have a shorter wavelengths, and thus are more sensitive to perturbation.

The mass-difference model is applied only to ThC because the phonon part of the thermal conductivity dominates at low temperatures. In the case of *fcc* thorium, an analogous model for electrons needs to be included, which is beyond the scope of this work.

Figures 21a and 21b show the reduction of the phonon thermal conductivity upon vacancies and oxygen. These impurities are incorporated into the 10 μm grain size model due to the greater proximity to the experimental samples [83].

It is confirmed that mass-difference defects have a negligible effect at higher temperatures, as they are overweighted by Umklapp scattering. The lifetimes of modes with high frequency and low group velocity are sharply reduced even with a small percentage of defects. Further addition of impurities has weaker effect as most sensitive modes have already reduced lifetimes.

Comparison of Figs. 21a and 21b suggests that the mass term is not so important because it is overweighted by the group velocity and the frequency with 3 and 4 power dependencies. Although vacancy has bigger mass-difference than oxygen, its phonon thermal conductivities are only slightly lower.

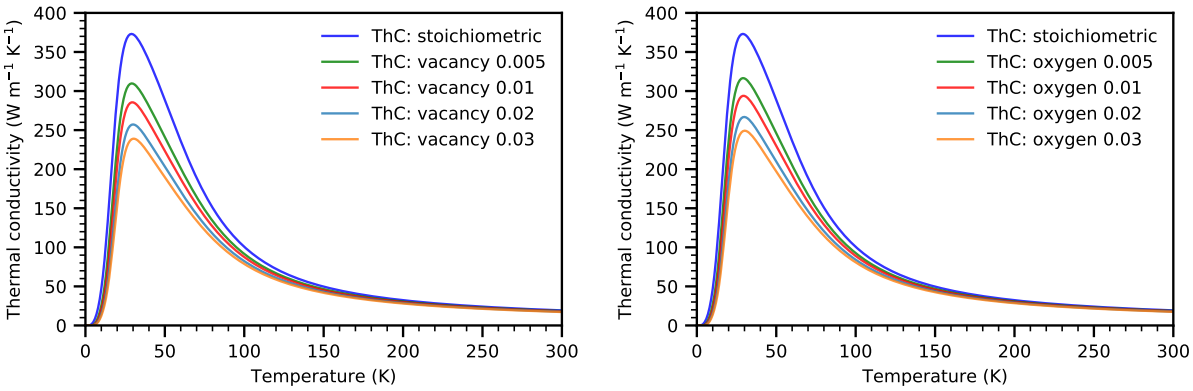

(a) vacancy defects

(b) oxygen defects

Figure 21: The phonon thermal conductivity for ThC (PBEsol+SOC+U_{eff} = 3 eV) with 10 μm grain size and defects.

However, it should be emphasized that this model is very simplified, and much more complex modeling needs to be used for accurate point defect modeling.

5 Conclusions

The electronic structure, elastic properties, lattice dynamics, and thermal conductivity of *fcc* thorium and thorium monocarbide (rocksalt structure) have been analyzed within the inclusion of the spin-orbit coupling with the use of Density Functional Theory.

Concerning *fcc* thorium, the spin-orbit coupling does not influence the electronic DOS at the vicinity of the Fermi energy formed mainly by the $6d$ and $5f$ states. However, a significant splitting of the $6p$ states is observed.

The analysis of *fcc* Th mechanical properties suggests that it is necessary to increase the occupation of the $6d$ states at the expense of the $5f$ states to reproduce the experimental elastic properties. The incorrect description of the $6p_{1/2}$ states caused by not using a relativistic basis may be the cause of undervalued theoretical c_{12} and overvalued c_{44} elastic constants.

The changes resulting from the addition of the SOC to the $6d$ states and the $5f$ states are negligible. Only the SOC acting on the $6p$ states can be important for some properties. Nevertheless, for lattice dynamics, the importance of the SOC has not been proved and may be neglected in the theoretical calculations for *fcc* thorium.

Different behavior is found in thorium monocarbide. The electronic density of states at the vicinity of the Fermi energy is indirectly modified by including the SOC on the $6p$ states. It yields a worse the Sommerfeld coefficient in comparison with the experiments. The same deterioration can be found for the bulk modulus. The importance of the SOC acting on the $6d$ states and the $5f$ states is not found.

The breaking point is the analysis of the phonon density of states. It is not possible to reproduce the optical phonon branches with or without the SOC. The mismatch between the theory and the experiment is more than 1.5 THz for ThC. The same problem is reported for uranium monocarbide. The only solution to get agreement with the experiment is adding the Hubbard model acting on the $5f$ states. This is an unconventional solution because thorium has very few occupied $5f$ states, and therefore there is no physical reason to increase on-site Coulomb repulsion. It is more of an artificial correction. However, this correction gives excellent agreement with the experimental phonon DOS.

Since the simple DFT with the second variational approach fails to predict the phonon spectrum, it raises the question of whether the precise description of the $6p$ states is needed or the description of the $5f$ electrons is insufficient even at such a low occupation.

The last part of work concerns the thermal conductivity. First, the theory is validated by the good agreement with the experimental values for *fcc* thorium. Then the comparison between Th and ThC is provided. It varies considerably because the total thermal conductivity of thorium is more than twice as large as that of ThC due to the much larger electron part of the thermal conductivity. The electronic part of the thermal conductivity of ThC is smaller due to weaker metallicity.

From the detailed analysis of the ThC phonon thermal conductivity, it is shown that the acoustic branches contribute 94 % of the phonon thermal conductivity. It comes from small lifetimes of optical modes. This is a striking difference with respect to other actinide compound, *i. e.* NpO_2, where the optical branches contribute 27 % of the phonon thermal conductivity. Despite all this, ThC has the higher phonon thermal conductivity than NpO_2, and this shows the importance of the acoustic branches. Higher thermal conductivity allows higher operational temperatures and therefore higher efficiency of IV. nuclear reactors.

The final analysis of grain boundary and mass-difference defects confirms that both defects are important only at low temperatures. They can be neglected for ambient temperature where the Umklapp scattering already prevails.

Publications

This work was published as *Lattice dynamics and thermal properties of thorium metal and thorium monocarbide* in Phys. Rev. B. 2020, **101**, 075117, 2020. DOI: 10.1103/physrevb.101.075117.

In connection with this topic, the following articles were further published during the study:

- HAVELA L., M. PAUKOV, M. DOPITA, L. HORÁK, D. DROZDENKO, M. DIVIŠ, I. TUREK, D. LEGUT, L. KÝVALA, T. GOUDER, A. SEIBERT, and F. HUBER. *Crystal structure and magnetic properties of uranium hydride UH_2 stabilized as a thin film.* Inorganic Chemistry 2018, **57**(23), 14727–14732. DOI: 10.1021/acs.inorgchem.8b02499
- PRCHAL J., V. BUTURLIM, J. VALENTA, M. DOPITA, M. DIVIŠ, I. TUREK, L. KÝVALA, D. LEGUT, and L. HAVELA, *Pressure variations of the 5f magnetism in UH_3*, Journal of Magnetism and Magnetic Materials 2020, **497**, 165993. DOI: 10.1016/j.jmmm.2019.165993
- HAVELA L., M. PAUKOV, M. DOPITA, L. HORÁK, M. CIESLAR, D. DROZDENKO, P. MINAŘÍK, I. TUREK, M. DIVIŠ, D. LEGUT, L. KÝVALA, T. GOUDER, F. HUBER, A. SEIBERT, and E. TERESHINA-CHITROVA, *XPS, UPS, and BIS study of pure and alloyed β-UH_3 films: Electronic structure, bonding, and magnetism.* Journal of Electron Spectroscopy and Related Phenomena. 2020, **239**, 146904. DOI: 10.1016/j.elspec.2019.146904
- KÝVALA L., M. TCHAPLIANKA, A. B. SHICK, S. KHMELEVSKYI, and D. LEGUT, *Large uniaxial magnetic anisotropy of hexagonal Fe-Hf-Sb alloys*, Crystals 2020, **10**, 430. DOI: 10.3390/cryst10060430

Acknowledgement

This master thesis was supported by the European Regional Development Fund in the IT4Innovations national supercomputing center - Path to Exascale project, No. CZ.02.1.010.00.016_0130001791 within the Operational Programme Research Development and Education and by Czech Science Foundation project No. 17 − 27790S.

References

[1] SINGH David. *Planewaves, pseudopotentials, and the LAPW method*. New York: Springer, 2006. ISBN: 978-0-387-29684-5.

[2] KAXIRAS Efthimios. *Atomic and Electronic Structure of Solids*. Cambridge: Cambridge University Press, 2003. ISBN: 978-0-511-07809-5.

[3] MARTIN M. Richard. *Electronic Structure*. Cambridge: Cambridge University Press, 2004. ISBN: 978-0-521-53440-6.

[4] TRITT Terry. *Thermal Conductivity: Theory, Properties, and Applications*. Boston: Springer US, 2004. ISBN: 0-306-48327-0.

[5] Wikipedia, the free encyclopedia. Umklapp scattering, 2020. [Online; accessed June 5, 2020].

[6] KÝVALA L. and D. LEGUT. Lattice dynamics and thermal properties of thorium metal and thorium monocarbide. *Physical Review B*, 101:075117, 2020. DOI: 10.1103/PhysRevB.101.075117.

[7] BAER Y. and J. K. LANG. High-energy spectroscopic study of the occupied and unoccupied 5f and valence states in Th and U metals. *Physical Review B*, 21(6):2060–2062, 1980. DOI: 10.1103/physrevb.21.2060.

[8] REESE R. A. et al. Phonon spectrum of thorium. *Physical Review B*, 8(4):1332–1337, 1973. DOI: 10.1103/physrevb.8.1332.

[9] WEDGWOOD F. A. Actinide chalcogenides and pnictides. III. optical-phonon frequency determination in UX and ThX compounds by neutron scattering. *Journal of Physics C: Solid State Physics*, 7(18):3203–3218, 1974. DOI: 10.1088/0022-3719/7/18/006.

[10] SCHETLERR H. G. et al. Thermal conductivity of high-purity thorium. *Physical Review*, 187(3):801–804, 1969. DOI: 10.1103/physrev.187.801.

[11] ANDERSON R. L. et al. 9th conference on thermal conductivity. Number Rept. CONF-691002, 1969.

[12] MARSH L. L. and J. R. KEELER. *The technology of thorium*. Number OCLC: 920699472 in BMI-76. Washington D.C: U.S. Atomic Energy Commission, 1951.

[13] VVEDENSKY D. D. *Quantum Theory of Electrons in Solids*. London: Imperial College, 2001.

[14] MORIN J. *Density functional theory: principles, applications and analysis*. New York: Nova Science Publishers Inc., 2013. ISBN: 978-1624179549.

[15] BURKE K. *The ABC of DFT.* New Jersey: Rutgers University, 2007.

[16] BLUNDELL S. J. *Magnetism: A Very Short Introduction.* Oxford: Oxford University Press, 2012. ISBN: 0199601208.

[17] DUDAREV et al. Electron-energy-loss spectra and the structural stability of nickel oxide: An LSDA+U study. *Physical Review B*, 57:1505–1509, 1998. DOI: 10.1103/PhysRevB.57.1505.

[18] HUBBARD J. Electron correlations in narrow energy bands. *Proceedings of the Royal Society of London. Series A. Mathematical and Physical Sciences*, 276(1365):238–257, 1963. DOI: 10.1098/rspa.1963.0204.

[19] PAVARINI E. *Correlated electrons: from models to materials lecture notes of the Autumn School Correlated Electrons 2012 at Forschungszentrum Jülich, 3-7 September 2012.* Jülich: Forschungszentrum Jülich, Zentralbibliothek, Verl, 2012.

[20] LIECHTENSTEIN A. I. et al. Density-functional theory and strong interactions: Orbital ordering in Mott-Hubbard insulators. *Physical Review B*, 52:R5467–R5470, 1995. DOI: 10.1103/PhysRevB.52.R5467.

[21] SIMON S. H. *The Oxford solid state basics.* Oxford: Oxford Univ. Press, 2013. ISBN: 978-0199680771.

[22] GRIMVALL G. *Thermophysical Properties of Materials.* Amsterdam: North Holland, 1999. ISBN: 0-444-82794-3.

[23] TOGO A. and I. TANAKA. First principles phonon calculations in materials science. *Scripta Materialia*, 108:1–5, 2015. DOI: 10.1016/j.scriptamat.2015.07.021.

[24] BROGLIA R. A. et al. *Solid State Physics of Finite Systems.* Berlin: Springer Berlin Heidelberg, 2004. ISBN: 978-3-662-09938-4.

[25] DOVE M. T. *Introduction to Lattice Dynamics.* Cambridge: Cambridge University Press, 1993. ISBN: 0-521-39293-4.

[26] ALVAREZ P. T. *Thermal Transport in Semiconductors.* Cham: Springer International Publishing, 2018. ISBN: 978-3-319-94983-3.

[27] VAN DEN EYNDE J-B. *Influence of the relaxation time approximation on first principle study of transport coefficients in thermoelectric material PbTe.* Louvain: Université catholique de Louvain, 2003.

[28] TOGO A. et al. Distributions of phonon lifetimes in brillouin zones. *Physical Review B*, 91:094306, 2015. DOI: 10.1103/PhysRevB.91.094306.

[29] ZLATIČ V. and R. MONNIER. *Modern Theory of Thermoelectricity*. Oxford: Oxford University Press, 2014. ISBN: 978–0–19–870541–3.

[30] MANES L., editor. *Actinides — Chemistry and Physical Properties*. Berlin: Springer Berlin Heidelberg, 1985. ISBN: 10.1007/3-540-13752-1.

[31] MORSS L. R. et al., editor. *The Chemistry of the Actinide and Transactinide Elements*. Springer Netherlands, 2006. ISBN: 10.1007/1-4020-3598-5.

[32] WILLS M. et al. *Challenges in Plutonium Science*, volume 1. Los Alamos: Los Alamos Science, 2012.

[33] COTTON S. A. *Lanthanide and actinide chemistry*. Chichester: Wiley, 2006. ISBN: 9780470010082.

[34] CLARK D. The chemical complexities of plutonium. *Los Alamos Sci.*, 26, 2000.

[35] JOHANSSON B. et al. Anomalous fcc crystal structure of thorium metal. *Physical Review Letters*, 75(21):3968–3968, 1995. DOI: 10.1103/physrevlett.75.3968.

[36] ABRAM T. and S. ION. Generation-IV nuclear power: A review of the state of the science. *Energy Policy*, 36(12):4323–4330, 2008. DOI: 10.1016/j.enpol.2008.09.059.

[37] IAEA. *Thorium Fuel Cycle - Potential Benefits And Challenges*. Number 1450 in IAEA TECDOC Series. Vienna: International Atomic Energy Agency, 2005.

[38] MANARA D. et al. Thermodynamic and thermophysical properties of the actinide carbides. In *Comprehensive Nuclear Materials*, pages 87–137. Elsevier, 2012.

[39] WANG Ch. et al. Defect stability in thorium monocarbide: An ab initio study. *Chinese Physics B*, 24(9):097101, 2015. DOI: 10.1088/1674-1056/24/9/097101.

[40] GREINER J. D. and J. F. SMITH. Magnetic susceptibility of high-purity thorium. *Physical Review B*, 4(10):3275–3277, 1971. DOI: 10.1103/physrevb.4.3275.

[41] HERY Y. et al. Magnetic susceptibility of protactinium monocarbide. In *2. International conference on the electronic structure of the actinides*, number 13-16 September 1976, Wroclaw, 1976.

[42] KRESSE G. and J. FURTHMFÜLLER. Efficient iterative schemes for ab initio total-energy calculations using a plane-wave basis set. *Physical Review B*, 54:11169–11186, 1996. DOI: 10.1103/PhysRevB.54.11169.

[43] BLÖCHL P. E. Projector augmented-wave method. *Physical Review B*, 50:17953–17979, 1994. DOI: 10.1103/PhysRevB.50.17953.

[44] KRESSE G. and D. JOUBERT. From ultrasoft pseudopotentials to the projector augmented-wave method. *Physical Review B*, 59:1758–1775, 1999. DOI: 10.1103/PhysRevB.59.1758.

[45] PERDEW J. P. et al. Generalized gradient approximation made simple. *Phys. Rev. Lett.*, 77:3865–3868, 1996. DOI: 10.1103/PhysRevLett.77.3865.

[46] PERDEW J. P. et al. Restoring the density-gradient expansion for exchange in solids and surfaces. *Phys. Rev. Lett.*, 100:136406, 2008. DOI: 10.1103/PhysRevLett.100.136406.

[47] VAN DER MAREL D. and G. A. SAWATZKY. Electron-electron interaction and localization in d and f transition metals. *Physical Review B*, 37:10674–10684, 1988. DOI: 10.1103/PhysRevB.37.10674.

[48] MADSEN G. K. H. et al. BoltzTraP2, a program for interpolating band structures and calculating semi-classical transport coefficients. *Computer Physics Communications*, 231:140–145, 2018. DOI: 10.1016/j.cpc.2018.05.010.

[49] VINET P. et al. Compressibility of solids. *Journal of Geophysical Research*, 92(B9):9319, 1987. DOI: 10.1029/jb092ib09p09319.

[50] LE PAGE Y. and P. SAXE. Symmetry-general least-squares extraction of elastic data for strained materials from ab initio calculations of stress. *Physical Review B*, 65(10), 2002. DOI: 10.1103/physrevb.65.104104.

[51] NORDSTRÖM L. et al. Spin-orbit coupling in the actinide elements: A critical evaluation of theoretical equilibrium volumes. *Physical Review B*, 63:035103, 2000. DOI: 10.1103/PhysRevB.63.035103.

[52] KUNEŠ J. et al. Electronic structure of fcc Th: Spin-orbit calculation with $6p_{1/2}$ local orbital extension. *Physical Review B*, 64:153102, 2001. DOI: 10.1103/PhysRevB.64.153102.

[53] WILLS J. M. et al. Density functional theory for d- and f-electron materials and compounds. *International Journal of Quantum Chemistry*, 116(11):834–846, 2016. DOI: 10.1002/qua.25097.

[54] SCHMIDT H. G. and G. WOLF. The heat capacity of Th and Th4H15 in the temperature range above 2 K. *Solid State Communications*, 16(9):1085–1087, 1975. DOI: 10.1016/0038-1098(75)90010-1.

[55] GORDON J. E. et al. Superconductivity of thorium and uranium. *Physical Review*, 152(1):432–437, 1966. DOI: 10.1103/physrev.152.432.

[56] GONZÁLEZ-CASTELAZO P. et al. Electron-phonon coupling and superconductivity in the light actinides: A first-principles study. *Physical Review B*, 93(10), 2016. DOI: 10.1103/physrevb.93.104512.

[57] GREINER J. D. et al. Comparison of the single-crystal elastic constants of Th and a ThC0.063 alloy. *Journal of Applied Physics*, 48(8):3357–3361, 1977. DOI: 10.1063/1.324221.

[58] SÖDERLIND P. et al. Elastic constants of cubic f-electron elements: Theory. *Physical Review B*, 48(13):9306–9312, 1993. DOI: 10.1103/physrevb.48.9306.

[59] SÖDERLIND P. Theoretical investigation of the high-pressure crystal structures of Ce and Th. *Physical Review B*, 52(18):13169–13176, 1995. DOI: 10.1103/physrevb.52.13169.

[60] BOUCHET J. and R. C. ALBETS. Elastic properties of the light actinides at high pressure. *Journal of Physics: Condensed Matter*, 23(21):215402, 2011. DOI: 10.1088/0953-8984/23/21/215402.

[61] GUPTA S. C. et al. Experimental and theoretical investigations on d and f electron systems under high pressure. *Metallurgical and Materials Transactions A*, 39(7):1593–1601, 2007. DOI: 10.1007/s11661-007-9377-1.

[62] BARIA J. K. and A.R. JANI. Lattice dynamics of La, Yb, Ce and Th. *Physica B: Condensed Matter*, 405(8):2065–2071, 2010. DOI: 10.1016/j.physb.2010.01.104.

[63] HU C. et al. Phase transition and thermodynamics of thorium from first-principles calculations. *Solid State Communications*, 150(9-10):393–398, 2010. DOI: 10.1016/j.ssc.2009.11.042.

[64] JAROSZEWICZ S. et al. The temperature behaviour of the elastic and thermodynamic properties of fcc thorium. *Journal of Nuclear Materials*, 429(1-3):136–142, 2012. DOI: 10.1016/j.jnucmat.2012.05.043.

[65] ARMSTRONG P. E. et al. Elastic constants of thorium single crystals in the range 77-400 K. *Journal of Applied Physics*, 30(1):36–41, 1959. DOI: 10.1063/1.1734971.

[66] WDOVIK U. D. et al. Effect of spin-orbit and on-site coulomb interactions on the electronic structure and lattice dynamics of uranium monocarbide. *Physical Review B*, 94(5), 2016. DOI: 10.1103/physrevb.94.054303.

[67] HARNESS J. B. et al. The specific heat of some uranium and thorium carbides between 1.8 K and 4.2 K. *British Journal of Applied Physics*, 15(8):963–966, 1964. DOI: 10.1088/0508-3443/15/8/313.

[68] DANAN J. Chaleur specifique de 2 a 300 K du monocarbure de thorium. *Journal of Nuclear Materials*, 57(3):280–282, 1975. DOI: 10.1016/0022-3115(75)90211-1.

[69] GERWARD L. et al. Compression of ThC to 50 GPa. *Journal of the Less Common Metals*, 161(1):L11–L14, 1990. DOI: 10.1016/0022-5088(90)90330-m.

[70] YU C. et al. Structural phase transition of ThC under high pressure. *Scientific Reports*, 7(1), 2017. DOI: 10.1038/s41598-017-00226-4.

[71] OLSEN J. S. et al. High-pressure structural studies of uranium and thorium compounds with the rocksalt structure. *Physica B*, 139-140:308–310, 1986. DOI: 10.1016/0378-4363(86)90584-x.

[72] SHEIN. I. R. and A. L. IVANOVSKII. Effect of spin-orbit coupling on structural, electronic, and mechanical properties of cubic thorium monocarbide ThC. *Physics of the Solid State*, 52(10):2039–2043, 2010. DOI: 10.1134/s1063783410100069.

[73] AYDIN S. et al. A theoretical study for thorium monocarbide (ThC). *Journal of Nuclear Materials*, 429(1-3):55–69, 2012. DOI: 10.1016/j.jnucmat.2012.05.038.

[74] DAROCA D. P. et al. Phonon spectrum, mechanical and thermophysical properties of thorium carbide. *Journal of Nuclear Materials*, 437(1-3):135–138, 2013. DOI: 10.1016/j.jnucmat.2013.01.350.

[75] SAHOO B. D. et al. Prediction of new high pressure structural sequence in thorium carbide: A first principles study. *Journal of Applied Physics*, 117(18):185903, 2015. DOI: 10.1063/1.4920929.

[76] STREET R. S. and T. N. WATERS. In *The thermal expansion of ThC and ThN*. Harwell: Energy Research Establishment, 1962.

[77] KUTTY T. R. et al. Thermophysical properties of thoria-based fuels. In *Thoria-based Nuclear Fuels*, pages 11–70. Springer London, 2013.

[78] SAHU P. Ch. et al. Electrical resistivity of thorium up to 10 GPa and 1300 K. *Physica B: Condensed Matter*, 160(2):177–182, 1989. DOI: 10.1016/0921-4526(89)90054-9.

[79] HAEN P. and G. T. MEADEN. The thermal conductivity, thermoelectric power, and electrical resistivity of thorium between 5 and 100 K. *Cryogenics*, 5(4):194–198, 1965. DOI: 10.1016/0011-2275(65)90056-1.

[80] AUSKERN A. B. and S. Aronson. Electrical properties of nonstoichiometric thorium carbides. *Journal of Applied Physics*, 38(9):3508–3514, 1967. DOI: 10.1063/1.1710161.

[81] CHIOTTI P. et al. Electrical resistivity and phase relations for the thorium-carbon system. *Journal of Nuclear Materials*, 23(1):55–67, 1967. DOI: 10.1016/0022-3115(67)90131-6.

[82] MALDONADO P. et al. Crystal dynamics and thermal properties of neptunium dioxide. *Physical Review B*, 93(14), 2016. DOI: 10.1103/physrevb.93.144301.

[83] OH J-Y. et al. Simulation of high burn up structure in UO2 using potts model. *Nuclear Engineering and Technology*, 41:1109, 2009. DOI: 10.5516/NET.2009.41.8.1109.